Agricultural and Forest Meteorology 366 (2025) 110468

Contents lists available at ScienceDirect

Agricultural and Forest Meteorology

journal homepage: www.elsevier.com/locate/agrformet

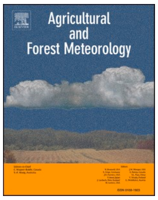

A novel approach for estimating evapotranspiration by considering topographic effects in radiation over mountainous terrain

Yixiao Zhang [a], Tao He [a,*], Shunlin Liang [b], Yichuan Ma [a,b], Yunjun Yao [c]

[a] *Hubei Key Laboratory of Quantitative Remote Sensing of Land and Atmosphere, School of Remote Sensing and Information Engineering, Wuhan University, Wuhan 430079, China*
[b] *Department of Geography, The University of Hong Kong, Hongkong 999077, China*
[c] *State Key Laboratory of Remote Sensing Science, Faculty of Geographical Science, Beijing, Normal University, Beijing 100875, China*

ARTICLE INFO

Keywords:
Evapotranspiration
Topographic effects
Landsat 8
TEEB

ABSTRACT

Mountains are one of the hotspots of climate change, and their complex morphology makes the monitoring of water and energy fluxes extremely challenging. Evapotranspiration (*ET*) is a crucial component of the water cycle and energy budget and its accurate estimation is essential for water resources management and ecosystem protection in mountains. It has been reported that the topography substantially controls the distribution of *ET* in mountainous terrain. However, most of the existing models neglect the impact of topography, leading to considerable errors and deviations for *ET* simulation. To address this issue, this study proposed a terrain-extended *ET* model (TEEB) based on the principle of energy balance, which can be used for *ET* estimation over complex terrains. Given the substantial impact of topography on net shortwave radiation (*NSR*), the mountain radiative transfer scheme was employed for *NSR* estimation, the net radiation model considering topographic effects was then constructed. Soil heat flux and sensible heat flux were then estimated from net radiation. The proposed TEEB model was tested using data from seven eddy covariance (EC) flux towers and a multidimensional comparison was made with the most widely used Surface Energy Balance Algorithm for Land (SEBAL) model. Regarding the results, the simulation of the TEEB model had a high consistency with EC measurements, with a root-mean-square-error of 0.713 mm/d, and was significantly superior to the SEBAL model. Moreover, the spatial pattern of estimated *ET* with the TEEB model exhibited distinct topographic characteristics, such as the *ET* on shady slopes being much lower than on sunlit slopes. Meanwhile, topographic analyses revealed that *ET* estimates on shady slopes would be reduced by 46 % with a proper consideration of topographic effects. The TEEB model can improve the estimation accuracy of *ET* in mountains, and provide a useful reference for maintaining ecological balance and optimizing water resources management.

1. Introduction

Mountain areas cover approximately 23 % of the global land surface (Grêt-Regamey and Weibel, 2020). Due to their critical role in providing freshwater for the adjacent areas downstream, mountains are often referred to as the world's water towers (Immerzeel et al., 2020;Immerzeel et al., 2010;Viviroli et al., 2007). Additionally, mountain ecosystems provide numerous ecological services, such as water conservation, fertilization and oxygen release (Briner et al., 2013;Grêt-Regamey and Weibel, 2020;Wang et al., 2018). Mountain areas, however, are highly sensitive to climate change (Immerzeel et al., 2020). Climate change threatens entire mountain ecosystems. Worldwide, the areas of snow cover are decreasing (Gisolo et al., 2022), glaciers are melting (Gisolo et al., 2022), and droughts are becoming more frequent (Beniston and Stoffel, 2014;Gobiet et al., 2014), all of which have an impact on the availability of water resources in mountainous areas. Evapotranspiration (*ET*), an important part of water resource consumption, links the water cycle and surface energy balance (Carter and Liang, 2019;Fisher et al., 2017;Hoek van Dijke et al., 2020). In the context of climate change, the determination of *ET* can help understand the characteristics of microclimate, and guide the ecological protection and water resources allocation in mountains (Chen et al., 2023;Gisolo et al., 2022).

Accurate determination of *ET* is a challenge (Fisher et al., 2017;Yang et al., 2019), especially in mountainous terrain. The Sixth Assessment

---

* Corresponding author at: Hubei Key Laboratory of Quantitative Remote Sensing of Land and Atmosphere, School of Remote Sensing and Information Engineering, Wuhan University, Wuhan, China.

E-mail address: taohers@whu.edu.cn (T. He).

https://doi.org/10.1016/j.agrformet.2025.110468
Received 15 July 2024; Received in revised form 22 February 2025; Accepted 23 February 2025

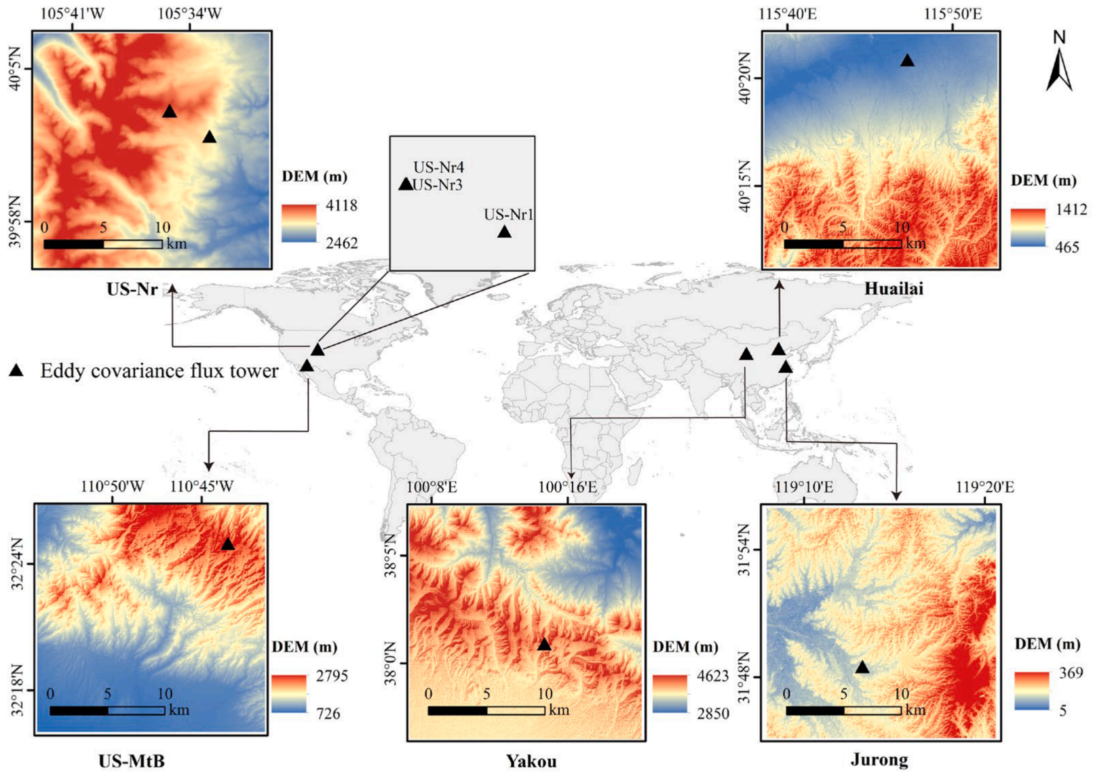

Fig. 1. Location of the eddy covariance flux stations within the study area.

Report contributed by the Intergovernmental Panel on Climate Change reported that the uncertainty range of global latent heat flux was 72–85 W/m^2 (5–95 % confidence range) (Forster et al., 2021). Studies have shown that this uncertainty in mountainous areas is larger (Jia et al., 2012;Yoon et al., 2019). For example, Xu et al. (2019) analyzed the relative uncertainties of *ET* products grid by grid over the conterminous United States (CONUS) and found that all *ET* products have higher relative uncertainties in west mountain areas than in the east of CONUS. The topographic effect on shortwave radiation is one of the reasons leading to higher uncertainties of *ET* products over mountain areas. Similarly, Hua et al. (2020) reported that the Penman-Monteith method significantly overestimated the potential evapotranspiration in the mountainous, with an average annual overestimation of 5 %. Generally, direct methods for measuring *ET* include lysimeter, Bowen-ratio, scintillometer, and eddy covariance (EC) technique (Pütz et al., 2016;Zhao et al., 2021), with EC measurement being considered the most accurate (Li et al., 2022). However, the direct determination of *ET* has limited spatial representativeness and the operational costs of instruments are expensive (Chang et al., 2017;Liu et al., 2018b;Wang et al., 2022). Furthermore, the density of ground sites established in mountainous areas is lower than that in flat areas (Wang et al., 2022). All these factors make the determination of regional *ET* difficult, especially in mountainous areas. The development of satellite remote sensing technology, with its extensive spatial coverage and low cost, offers an unprecedented opportunity for modeling regional *ET*. There are a large number of models for *ET* estimation based on remote sensing techniques, from statistical and empirical methods that relate *ET* to surface parameters (Barzkar et al., 2021;Carter and Liang, 2019;Douna et al., 2021;Jackson et al., 1977), to physical models that calculate *ET* as the residual of the surface energy balance, such as the Surface Energy Balance System (Ershadi et al., 2013;Su, 2002), the Surface Energy Balance Algorithm for Land (SEBAL) (Bastiaanssen et al., 1998;Tang et al., 2013), the Two Source Energy Balance (Norman et al., 1995), the Two Source Trapezoid Model for Evapotranspiration (Long and Singh, 2012), and the Hybrid dual source scheme and Trapezoid framework-based Evapotranspiration Model (Yang and Shang, 2013). However, most of the existing models are designed for flat areas without topographic consideration and cannot be used directly in mountainous areas (Bastiaanssen et al., 1998; Gao et al., 2008).

The surface energy fluxes in complex terrain exhibit different characteristics compared to flat areas (Gao et al., 2008;Wang et al., 2022). For example, surface net radiation, the energy source for *ET*, varies not only with altitude but also significantly between shady and sunlit slopes (Holland and Steyn, 1975). This variation directly affects the magnitude and spatial distribution of *ET* (Gao et al., 2008). The remote sensing retrieval of *ET* in complex terrain is complicated due to the difficulty in estimating net radiation at different slopes and azimuths as well as the uncertainty in the energy transport process (Wang et al., 2022). However, neglecting topographic effects (e.g., slope, aspect, and elevation) introduces considerable errors in *ET* estimates. Previous research had directly demonstrated that *ET* would be overestimated by 30 % in a high altitude, shady slope region if the SEBAL model was used without considering topography (Liu et al., 2008). Similarly, Ma et al. (2023b) improved the sensible heat flux calculation and found that although the *ET* simulation accuracy was improved over the original model, the deviations and errors were still high when applied in mountainous areas. Therefore, it is essential to consider topographic effects when estimating *ET* in mountainous terrain.

Existing studies on *ET* estimation over mountainous terrain are limited. Although a few methods have been developed to obtain *ET* with topographic consideration (Gisolo et al., 2022;McVicar et al., 2007; Wang et al., 2022), most of them require sufficient ground-based observations and are hard to apply in mountainous areas owing to the lack of ground stations. For example, Wang et al. (2022) calculated *ET* under complex topographic conditions; however, observation data were needed to calibrate the solar radiation model. This hinders the use of this method in areas where ground-based observations are unavailable. In addition, the net radiation drives the *ET* process and its accuracy is critical for *ET* calculation. As far as *ET* estimation over mountainous terrain is concerned, the prevailing approaches are still topographic

Table 1
Information for the eddy covariance flux towers.

Site	Country	Latitude	Longitude	Elevation	LULC	Slope	Aspect
US-Nr1	USA	40°1′58″ N	105°32′47″ W	3050 m	ENF	4.8°	90.0°
US-Nr3	USA	40°3′7″ N	105°35′11″ W	3504 m	GRA	3.4°	123.7°
US-Nr4	USA	40°3′7″ N	105°35′9″ W	3502 m	GRA	8.2°	125.5°
US-MtB	USA	32°24′58″ N	110°43′34″ W	2573 m	ENF	2.0°	180.0°
Yakou	China	38°0′50″ N	100°14′31″ E	4148 m	GRA	2.1°	333.4°
Jurong	China	31°48′25″ N	119°13′2″ E	15 m	CRO	2.1°	333.4°
Huailai	China	40°20′57″ N	115°47′17″ E	480 m	CRO	3.0°	108.4°

Note: LULC, land use/cover; ENF, evergreen needleleaf forest; GRA, grasslands; CRO, cropland.

correction for solar radiation (Aguilar et al., 2010;Allen et al., 2007; Chen et al., 2013). Allen et al. (2007) improved the calculation of solar radiation in the SEBAL energy balance process by correcting the solar incidence angle using declination, latitude, slope, and aspect. Chen et al. (2013) calibrated solar radiation using topography and separately calculated direct radiation, diffuse radiation, and reflected radiation from surrounding environment. However, atmospheric radiative process and topographic effects are coupled, making topographic correction unreliable (Ma et al., 2023a;Zhang et al., 2019). To address the above limitations, a terrain-extended *ET* model (TEEB) based on the principle of energy balance is constructed to estimate *ET* over mountainous terrain.

The objectives of this study are: 1) to develop an improved parameterization model for *ET* estimation over mountainous terrain; 2) to evaluate the performance of the proposed model based on the flux tower observations; 3) to explore the impact of topographic factors on *ET* estimation. This study is structured as follows. Section 2 presents the selected study areas and data. In Section 3, the improved parameterization model considering topographic effects is proposed. In Section 4, we systematically evaluate the performance of the proposed model at the site, temporal, and spatial scales and we analyze the impact of the topographic effects on *ET*. Section 5 further explores the relative contributions of the topographic factors and discusses the uncertainties, advantages, and limitations of our approach. Finally, conclusions are presented in Section 6.

2. Materials

2.1. Eddy covariance stations description

Seven EC flux towers with different topographic conditions were utilized for model evaluation (Fig. 1 and Table 1): Mt. Bigelow (US-MtB), Niwot Ridge Alpine (T-Van west, US-Nr3), Niwot Ridge Alpine (T-Van east, US-Nr4), Niwot Ridge Forest (US-Nr1), Yakou observation site (Yakou), Huailai Remote Sensing Experiment site (Huailai), and Jurong Ecological Experimental Site (Jurong). Five sites (i.e., US-MtB, US-Nr3, US-Nr4, US-Nr1, and Yakou) are located in complex terrain, while two sites (i.e., Huailai and Jurong) are in relatively flat areas.

2.1.1. Mt.Bigelow (US-MtB)

The US-MtB site (https://ameriflux.lbl.gov/sites/siteinfo/US-MtB, last accessed Mar 29th, 2024) is located on the western slope of Mt. Bigelow in the Santa Catalina Mountains, which is about 29 km northeast of Tucson, Arizona, U.S. (Knowles et al., 2020). It is predominantly covered with evergreen needleleaf forest with an average canopy height of 10 m. The forest ecosystem comprises ponderosa pine (*Pinus ponderosa*), Mexican white pine (*Pinus strobiformis Engelmann*), Douglas fir (*Pseudotsuga menziesii*), Chihuahua pine (*Pinus leiophylla*), and southwestern white fir (*Pinus strobiformis Engelmann*). A semiarid climate characterizes the region, with a mean annual temperature of 9.3 °C and mean annual precipitation of approximately 790 mm.

2.1.2. Niwot ridge (US-Nr1, US-Nr3, US-Nr4)

Three sites on Niwot Ridge in the Colorado Rocky Mountains are located within the extent of the subalpine forest ecosystem and alpine tundra ecosystem. These sites include: US-Nr1 (https://ameriflux.lbl.gov/sites/siteinfo/US-NR1, last accessed Mar 29th, 2024), US-Nr3 (https://ameriflux.lbl.gov/sites/siteinfo/US-NR3, last accessed Mar 29th, 2024), and US-Nr4 (https://ameriflux.lbl.gov/sites/siteinfo/US-NR, last accessed Mar 29th, 2024). The US-Nr1 site is situated in evergreen needleleaf forests with a tree height of 12–13 m (Burns et al., 2015). It is classified as Dfc based on the Köppen-Geiger classification (Burns et al., 2015), representing a cold, snowy/moist continental climate. The mean annual precipitation is around 800 mm. The US-Nr3 is located 50 m west of the US-Nr4, and both sites are covered by grasslands. The mean annual temperature and precipitation at these sites are −2.2 °C and 884 mm, respectively. The Rocky Mountains block the prevailing westerly winds, resulting powerful down sloping winds at this location (Knowles et al., 2012).

2.1.3. Yakou observation site (Yakou)

The Yakou site (https://data.tpdc.ac.cn/, last accessed Mar 29th, 2024) belongs to the Qilian Mountainous integrated observatory network and is located in Qilian County, Qinghai Province, China. It is a typical alpine cold desert landscape and the predominant land use type is alpine meadow. This region experiences a pronounced continental climate, with mean annual precipitation ranging from 400 to 600 mm (Liu et al., 2018a). Due to its alpine ecosystem, the temperature can drop as low as −40 °C.

2.1.4. Huailai remote sensing experiment site (Huailai)

The Huailai site (https://data.tpdc.ac.cn/, last accessed Mar 29th, 2024) lies in the southwest of the Yanqing-Huailai basin, surrounded by mountains to the north and south sides. It experiences a temperate continental monsoon climate, with a long-term mean annual temperature of 10.0 °C and mean annual precipitation of 367.9 mm (Guo et al., 2020). The Huailai site is situated in cropland predominantly covered with corn.

2.1.5. Jurong ecological experimental site (Jurong)

Situated in the Middle-lower Yangtze Plain (Fig. 1), the Jurong site (http://www.nesdc.org.cn/, last accessed Mar 29th, 2024) experiences a subtropical subhumid monsoon climate characterized by four clearly distinct seasons, moderate climate and abundant rainfall. The soil texture is clay loam, and the site is established on irrigated cropland primarily used for rice cultivation.

2.2. Eddy covariance flux tower measurements

All the above sites utilize the EC system to continuously monitor energy and mass fluxes. Half-hourly data were provided by each site. Note that the half-hourly fluxes from the US-Nr1 site have been gap-filled by tower team. For other sites, there are some missing values in observation data. The percentage of the missing data at the seven sites was provided in the supplementary material (Table S1). Initially, the half-hourly data were filled using the mean diurnal variations (Falge et al., 2001a,b), and window sizes of 14 days and 7 days (Falge et al., 2001a) were selected for daytime and nighttime, respectively. Daily

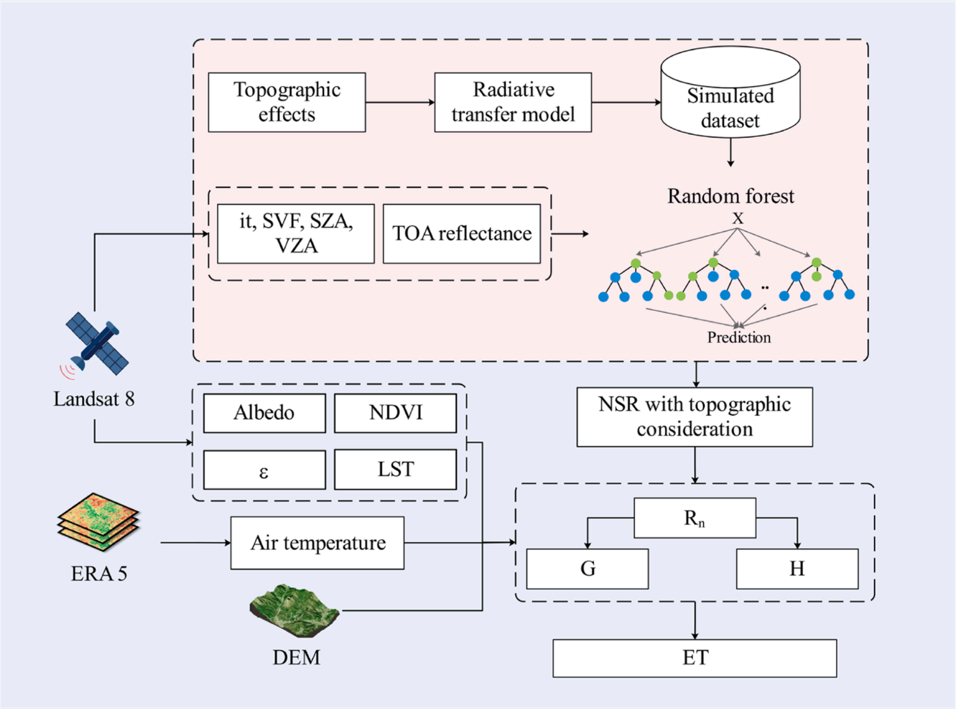

Fig. 2. Computational framework. 'it' refers to local incident angle; 'SVF' is sky view factor; 'SZA' denotes solar zenith angle; 'VZA' means view zenith angle; 'ε' represents land surface emissivity; 'LST' is land surface temperature.

fluxes from each site were aggregated from half-hourly fluxes after the gap-filling process. In addition, since the EC method suffers an energy imbalance problem (Twine et al., 2000), the Bowen ratio correction method (Castelli et al., 2018;Twine et al., 2000) was used to perform energy closure correction on a daily scale. Detailed information on the energy balance closure analysis was provided in the supplementary material (Table S2).

2.3. Landsat 8

The Landsat satellites series, known for their excellent image quality and rich spectral information, are widely used in various remote sensing applications (Anderson et al., 2012;Guo et al., 2022;Ma et al., 2023a). Landsat 8, launched in 2013 by the U.S. Geological Survey (USGS) and the National Aeronautics and Space Administration (NASA), has a revisit period of 16 days (Wulder et al., 2019). It is equipped with two sensors: the Operational Land Imager (OLI) and the Thermal Infrared Sensor (TIRS). The OLI consists of nine bands with a spatial resolution of 30 m (visible, NIR, SWIR) and 15 m (panchromatic). The TIRS divides a thermal infrared channel into two thermal infrared bands, enhancing the accuracy of thermal infrared parameter retrieval.

Given the impact of weather conditions on image quality and availability, a total of 138 images from 2013 to 2020 were selected in our study. The information on the selected images was shown in the supplementary material (Table S3), and all Landsat 8 images were obtained from the USGS (https://earthexplorer.usgs.gov/).

2.4. ERA5

The European reanalysis (ERA5)-Land reanalysis dataset (Muñoz-Sabater et al., 2021) is published by the European Center for Medium-Range Weather Forecasts (ECMWF) (https://www.ecmwf.int/en/forecasts/dataset/ecmwf-reanalysis-v5), and it is the fifth generation of global climate and weather reanalysis data. This dataset provides extensive climate data for atmosphere, land, and ocean. We downloaded the EAR5-land air temperature data with a temporal resolution of hourly and a spatial resolution of 0.1°. In addition, the data close to the overpass time of Landsat 8 were extracted to retrieve *ET*.

2.5. DEM data

ALOS Global Digital Surface Model "ALOS World 3D – 30m" (AW3D) with a spatial resolution of 30 m is the highest accurate 3D map in the world (Carrera-Hernandez, 2021). It was provided by Japan's Aerospace Exploration Agency (JAXA) (https://earth.jaxa.jp/en/).

3. Methodology

In this study, the TEEB model, which builds upon the principle of energy balance and couples a net radiation model with topographic consideration, was constructed to estimate *ET* in mountainous terrain (Fig. 2). Specifically, an extended direct estimation method was applied for net shortwave radiation (*NSR*) estimation, and then a net radiation model considering topographic effects was developed. The sensible heat flux (*H*) and soil heat flux (G) were directly linked to the net radiation results, incorporating topographic effects into *H* and G indirectly.

The surface energy balance equation is usually composed of latent heat flux, net radiation, *H*, and G:

$$\lambda ET = R_n - G - H \tag{1}$$

where λ is the latent heat of vaporization (kJ/kg), R_n is the net radiation flux (W/m^2), G is the soil heat flux (W/m^2), H is the sensible heat flux (W/m^2).

ET estimation herein can be separated into four steps (Fig. 2). Firstly, Landsat 8 and DEM were used to extract surface parameters (i.e., normalized difference vegetation index, surface temperature, emissivity, surface albedo), topography (i.e., local incident angle, sky view factor), and auxiliary information (i.e., solar zenith angle, view zenith angle). The air temperature was obtained from the ERA5 dataset. Secondly, a simulation database was constructed using the terrain-extended libRadtran (http://www.libradtran.org/doku.php) (Mayer and Kylling, 2005), and satellite top-of-atmosphere (TOA) reflectance, elevation, topography, and auxiliary information were linked with *NSR* through a random forest model (see Section 3.1). Thirdly, net radiation considering topographic effects was calculated using the radiative energy balance equation. *H* was determined through its nonlinear relationship with net radiation. Similarly, G was also acquired on the basis of net radiation (see Section 3.2 and Section 3.3). Finally, the instantaneous latent heat flux was derived using the surface energy balance equation. The daily *ET* was subsequently calculated under the assumption that the evaporation fraction remains constant throughout the day (see Section 3.4).

3.1. Instantaneous net radiation flux

In the TEEB model, the net radiation with topographic consideration is calculated as followed:

$$R_n = NSR + (Rl_{in} - Rl_{out}) - (1-\varepsilon)Rl_{in} \tag{2}$$

where *NSR* is the net shortwave radiation (W/m^2), Rl_{in} is the input longwave radiation (W/m^2), Rl_{out} is the output longwave radiation (W/m^2), and ε is the land surface emissivity (dimensionless):

$$\varepsilon = 0.004P_v + 0.986 \tag{3}$$

where P_v represents the fractional vegetation cover (dimensionless), it is determined by empirical equation according to the normalized difference vegetation index (*NDVI*):

$$P_v = \begin{cases} NDVI > 0.7 & 1 \\ NDVI < 0.05 & 0 \\ 0.05 <= NDVI <= 0.7 & (NDVI - 0.05)/(0.7 - 0.05) \end{cases} \tag{4}$$

For Rl_{out}, the following equation is adopted:

$$Rl_{out} = \varepsilon \times \sigma \times T_s^4 \tag{5}$$

where $\sigma$is the Stefan Boltzman constant (5.67×10^{-8} W/m^2/k^4), T_s is the surface temperature (K). According to Bastiaanssen et al. (1998), Rl_{in} is described as follows:

$$Rl_{in} = 1.08 \times (-In\tau_{sw})^{0.265} \times \sigma \times T_a^4 \tag{6}$$

where T_a is the air temperature (K), and τ_{sw} is the air atmospheric transmissivity expressed by the following equations:

$$\tau_{sw} = 0.75 + 2 \times 10^{-5} \times Z \tag{7}$$

where Z is the elevation (m).

For *NSR* estimation, the direct estimation method is one of the common approaches (Chen et al., 2022b;Kim and Liang, 2010), which was proposed by Liang et al. (1999). The core of this method is to create a simulated dataset of TOA reflectance and surface *NSR* under various typical atmospheric and surface characteristics through radiative transfer model. Then, a statistical relationship is established between TOA reflectance and *NSR* to estimate *NSR*. In this study, a direct estimation method with topographic consideration (Liang et al., 1999;Ma et al., 2023a) was implemented in our model, which consists of four steps, as described below.

Step 1. Topographic effects were coupled with libRadtran to obtain the terrain-extended radiative transfer model. The downward shortwave radiation (*DSR*) in mountainous terrain is divided into direct radiation (E_t^{dir}, W/m^2), diffuse radiation (E_t^{dif}, W/m^2), and reflected radiation from surrounding environment (E_t^{ref}, W/m^2), which can be expressed following Sandmeier and Itten (1997):

$$E_t^{dir} = \Theta \cdot E_h^{dir} \cdot (\cos i_t \,/\, \cos\omega) \tag{8}$$

$$E_t^{dif} = E_h^{dif} \cdot V_{sky} \tag{9}$$

$$E_t^{ref} = \overline{\alpha} \cdot (1 - \psi_{sky}) \cdot E_h \tag{10}$$

where Θ is the shadow factor (dimensionless), E_h^{dir} and $E_h^{dif}$are the direct radiation (W/m^2) and diffuse radiation (W/m^2) over the horizontal plane, respectively. E_h is the horizontal *DSR* (W/m^2), which is composed of $E_h^{dir}$and E_h^{dif}, ω is the solar zenith angle (SZA, °), V_{sky} is the sky view factor (SVF, dimensionless), $\overline{\alpha}$ is the average albedo of surrounding environment (dimensionless), i_t is the local incident angle (°), it is computed as follows (Hantson and Chuvieco, 2011;Horn, 1981):

$$\cos i_t = \cos\omega\cos\beta + \sin\omega\sin\beta\cos(\varphi_s - \varphi_0) \tag{11}$$

where β is the slope (°), φ_s is the solar azimuth angle (°), and φ_0 is the aspect (°). Further, surface *NSR* with topography can be obtained by:

$$E_t = E_t^{dir} + E_t^{dif} + E_t^{ref} \tag{12}$$

$$NSR = (1 - \alpha) \cdot E_t \tag{13}$$

where E_t is the *DSR* in mountains (W/m^2), α is the surface albedo (dimensionless).

The TOA reflectance can be achieved through the following way (Li et al., 2012;Ma et al., 2023a):

$$L_{TOA} = L_0 + E_t \frac{T_V}{\pi} \cdot \frac{\rho_m}{1 - S\rho_m} \tag{14}$$

$$\rho_{TOA} = \frac{L_{TOA} \cdot \pi \cdot d^2}{\cos\omega \cdot E_0} \tag{15}$$

where L_{TOA} is the TOA radiance (W/m^2), $L_0$is the path radiance (W/m^2), T_V is the total transmittance in the viewing direction (dimensionless), ρ_m is the Lambertian surface reflectance (dimensionless), S is atmospheric albedo (dimensionless) which is the bi-hemispherical ratio between upwelling radiation from the surface and the downwelling radiation (Li et al., 2010). ρ_{TOA} is the TOA reflectance (W/m^2), d is the Earth-Sun distance (dimensionless), and E_0 is the mean solar exoatmospheric irradiance (W/m^2) (Chander et al., 2009;Li et al., 2012).

Step 2. A simulated dataset considering different solar angles, atmosphere, surface, and terrain conditions was constructed based on Step 1. The radiative transfer model (i.e., libRadtran) was performed on a Linux system and the DISORT solver was used for simulation. The solar zenith angle was set to 0–80° (in steps of 10°), the view zenith angle was set to 0–20° (in steps of 10°), and the elevation was set as 0 km, 2 km, 4 km, 6 km, and 8 km. A library of 245 surface spectra collected from the Advanced Spaceborne Thermal Emission Reflection Radiometer (Baldridge et al., 2009) and the USGS (Clark et al., 2007) was used to characterize the surface conditions. The variations of aerosol optical depth (AOD) were considered in this process (Chen et al., 2022a), and the aerosol was set as “rural” type, with AOD at 550 nm was set as 0, 0.05, 0.1, 0.15, 0.2, 0.3, 0.4, and 0.6. The local incidence angle and SVF were used to characterize the topographic effects, where the local incidence angle was set to 0–90° (in steps of 10°) and SVF was set as 0.4, 0.7, and 1.0. The wavelength range of the simulated ground *NSR* was from 30 to 3000 nm, and the TOA reflectance simulation results were stored at 1 nm spectral resolution. Besides, the TOA reflectance of Landsat 8 was obtained using the corresponding spectral response function (SRF) (Barsi et al., 2014):

$$\rho_{TOA(i)} = \frac{\int_{\lambda_{\min}}^{\lambda_{\max}} SRF(\lambda)\rho(\lambda)d\lambda}{\int_{\lambda_{\min}}^{\lambda_{\max}} SRF(\lambda)d\lambda} \tag{16}$$

where $\rho_{TOA(i)}$ represents the TOA reflectance of Landsat 8 at band *i*, $\lambda_{\min}$ and $\lambda_{\max}$ are the minimum and maximum wavelengths of band *i*, $SRF(\lambda)$ and $\rho(\lambda)$ represent the SRF and TOA reflectance at the wavelength of λ, respectively.

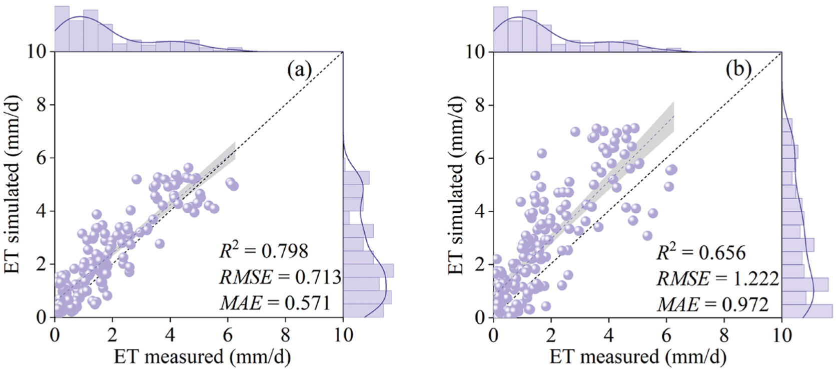

Fig. 3. Scatter of the measurement of the eddy flux tower with TEEB (a) and SEBAL (b) modeled *ET*. The histograms at the top and right in each sub-part represent the frequency distribution of *ET* measured and simulated, respectively.

Step 3. The random forest model was employed to establish the relationship between TOA reflectance and surface *NSR* based on the simulated dataset:

$$NSR = f(\omega, \theta_V, elevation, i_t, V_d, TOAreflectance) \quad (17)$$

where θ_V is the view zenith angle (VZA, °). 70 % simulations were selected to build random forest model, and 30 % were used to validate the model. The random forest model was implemented with the “scikit-learn” package (Pedregosa et al., 2011) (https://scikit-learn.org/stable/index.html) in Python. All parameters were set as default values.

Step 4. Landsat 8 TOA reflectance observations were applied for estimating surface *NSR* based on the trained random forest model.

3.2. Instantaneous sensible heat flux

The *H* typically needs to be calculated through iterations, which can introduce errors (Ma et al., 2023b;Rahimzadegan and Janani, 2019). Previous studies have demonstrated that there was an exponential relationship between *H* and net radiation, which has proven effective in improving the calculation of *H* and achieving satisfactory performance in simulating *ET* (Ma et al., 2023b;Nyambayo and Potts, 2010). Based on that, *H* can be estimated with the following equation:

$$H = a \times e^{b \times R_n} + c \quad (18)$$

Where R_n is the net radiation (W/m^2). The values of *a, b*, and *c* are taken as 115.1, 0.001629, and −171.4, respectively (Ma et al., 2023b).

3.3. Instantaneous soil heat flux

Although G is a relatively small part of the surface energy balance equation, it is difficult to calculate directly. It can be obtained as suggested by Bastiaanssen (2000):

$$G = \frac{T_s - 273.15}{\alpha} \times \left(0.0038 \times \alpha + 0.0074 \times \alpha^2\right) \times \left(1 - 0.98 \times NDVI^4\right) \times R_n \quad (19)$$

3.4. Daily evapotranspiration

According to Shuttleworth et al. (1989), evaporative fraction (*EF*) almost unchanged during the day. We used *EF* to expend the instantaneous *ET* to the daily:

$$EF = \frac{\lambda ET}{R_n - G} \quad (20)$$

$$ET_{24} = \frac{86400 \times EF \times R_{n24}}{\lambda} \quad (21)$$

where R_{n24} is the daily net radiation (W/m^2). λ is the latent heat of vaporization, it can be descripted as:

$$\lambda = [2.501 - 0.002361 \times (T_s - 273.15)] \times 10^6 \quad (22)$$

In the TEEB model, the R_{n24} can be estimated as:

$$R_{n24} = (1 - \alpha) \times R_{s24} - 110 \times \tau_{sw24} \quad (23)$$

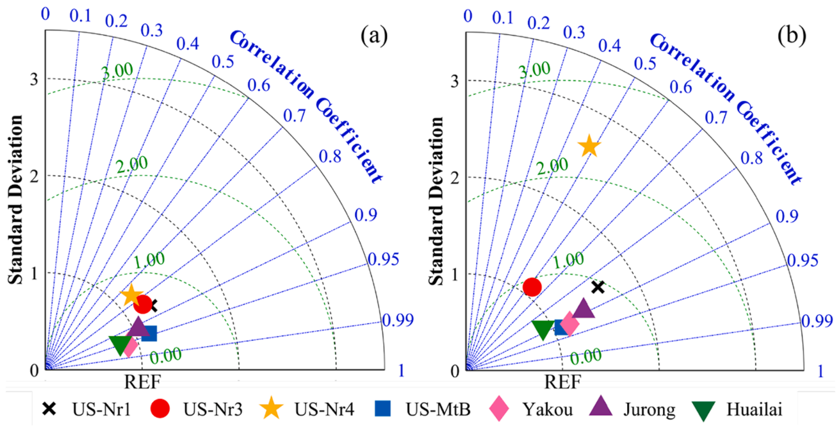

Fig. 4. Taylor diagrams that compared the performance of the TEEB (a) and SEBAL (b) models at all sites. The radial distance of the origin reflects standard deviation. The cosine of the azimuth angle indicates the correlation coefficient. The distance from the reference point (marked as REF on the x-axis) represents the RMSE.

Table 2
Comparison of the TEEB and SEBAL models at all flux towers.

Sites	TEEB			SEBAL		
	R^2	RMSE (mm/d)	MAE (mm/d)	R^2	RMSE (mm/d)	MAE (mm/d)
US-Nr1	0.730	0.892	0.705	0.716	1.163	0.906
US-Nr3	0.747	0.336	0.303	0.388	0.431	0.380
US-Nr4	0.575	0.449	0.330	0.233	1.361	0.763
US-MtB	0.891	0.441	0.358	0.834	0.524	0.391
Yakou	0.917	0.404	0.307	0.833	0.752	0.587
Jurong	0.841	0.529	0.434	0.796	0.780	0.632
Huailai	0.888	0.572	0.457	0.764	0.924	0.738

where τ_{sw24} is the mean daily atmospheric transmissivity, R_{s24} is the daily solar radiation. The solar radiation considering topographic effects over mountainous terrain is calculated using the procedure proposed by (Allen et al., 2006) for estimating daily solar radiation for inclined surfaces.

4. Results

4.1. Performance of the TEEB model

In this study, we developed the TEEB model for *ET* estimation in mountainous terrain. An overall evaluation of model output was performed in comparison with ground measurements for all days having remote sensing imagery, and the coefficient of determination (R^2), root mean square error (RMSE), and mean absolute error (MAE) were utilized as assessment indicators (Fig. 3). It was clear that there was a good agreement between the results of the TEEB model and observations, with a RMSE of 0.713 mm/d, an R^2 of 0.798, and a MAE of 0.571 mm/d. The SEBAL model exhibited inferior performance to the TEEB model. The corresponding statistics were 1.222 mm/d, 0.656, and 0.972 mm/d, respectively. Overall, the proposed TEEB model significantly enhanced *ET* estimation, with R^2 increased by about 2 % and the RMSE and MAE decreased by approximately 42 %. As for the SEBAL model, it ignored the illumination conditions differences in various aspects, leading to the incompatibility between low albedo and high incoming solar radiation. As a result, these areas were incorrectly assumed to be high absorbance areas, causing overestimation of *ET*.

The Taylor diagrams for both the TEEB and SEBAL models at all sites were presented in Fig. 4. A Taylor diagram is a polar-style graph showing the correlation coefficient, standard deviation, and RMSE between estimated values and observed values (Taylor, 2001). As shown in Fig. 4, the TEEB model performed the worst at US-Nr4 among all flux towers. One possible explanation is that this site is located in the alpine tundra areas, where the availability of data is limited and random errors are significantly greater due to topography and climate (Knowles et al., 2012). Compared to the SEBAL model, the RMSE for the TEEB model was smaller at all flux towers, with the average value decreasing from 0.848 mm/d to 0.518 mm/d. Similarly, the TEEB model had higher R^2 (0.798) and lower MAE (0.413 mm/d) (Table 2). In addition, the performance of the TEEB model in complex terrain (i.e., US-Nr1, US-Nr3, US-Nr4, US-MtB, and Yakou) was comparable to that over relatively flat areas (i.e., Jurong and Huailai). Specifically, the TEEB model in complex terrain obtained the average R^2, RMSE, and MAE of 0.772, 0.504 mm/d and 0.406 mm/d, respectively. In relatively flat areas, the corresponding values were 0.864, 0.551 mm/d and 0.446 mm/d, respectively. The TEEB model outperformed the SEBAL model over both the complex terrain and the relatively flat areas, which indicates that the proposed model was stable and robust.

To comprehensively assess the simulated *ET* accuracy of the TEEB model, we further divided the whole year into two distinct seasons: a warm season and a cold season. The warm season includes April, May, June, July, August, and September, while the rest of the months (i.e., January, February, March, October, November, and December) belong to the cold season. The RMSE values of the TEEB and SEBAL models in different seasons at all selected sites were shown in Fig. 5. Considering that only two days at US-Nr3 were in the warm season, US-Nr1, US-Nr3, and US-Nr4 were analyzed together here. The TEEB model exhibited satisfactory results in both warm and cold seasons, with average RMSE values of 0.409 mm/d and 0.441 mm/d, respectively; the corresponding RMSE values for the SEBAL model were 0.753 mm/d and 0.706 mm/d.

4.2. Capacity for the TEEB model to simulate ET

Fig. 6 presented the results of *ET* estimated using the TEEB model, which were plotted with corresponding *ET* measurements of EC towers. Overall, the *ET* derived by the TEEB model was closer to the measured values than those derived by the SEBAL model (Table 2 and Fig. 6). At all selected sites, the SEBAL model consistently exhibited a tendency to overestimate *ET*, while the TEEB model mitigated this overestimation. The estimation results revealed a pattern of relatively low *ET* at the beginning of the year, followed by a gradual increase and culminated in a peak in summer. This trend corresponds to the seasonal variation in vegetation growth (Ma et al., 2023b). It should be pointed out that although the results of the TEEB model were very close to the ground measurements (the RMSE values vary from 0.336 mm/d to 0.892 mm/d) and the patterns were largely consistent (Table 2 and Fig. 6), discrepancies between the estimated and measured values still existed. These discrepancies may be attributed to the simplifications inherent in the single-source model (Bastiaanssen et al., 1998;Gao et al., 2008), as well as potential measurement uncertainties.

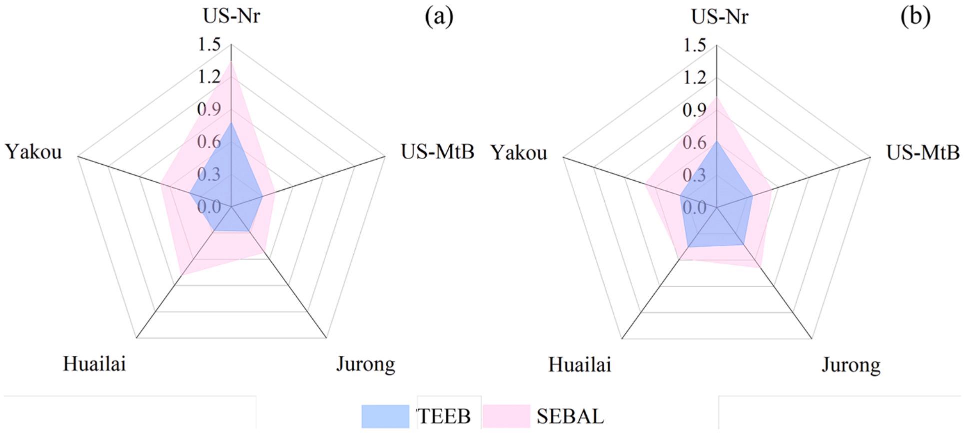

Fig. 5. The RMSE values of TEEB and SEBAL models in the warm season (a) and cold season (b) at all flux towers.

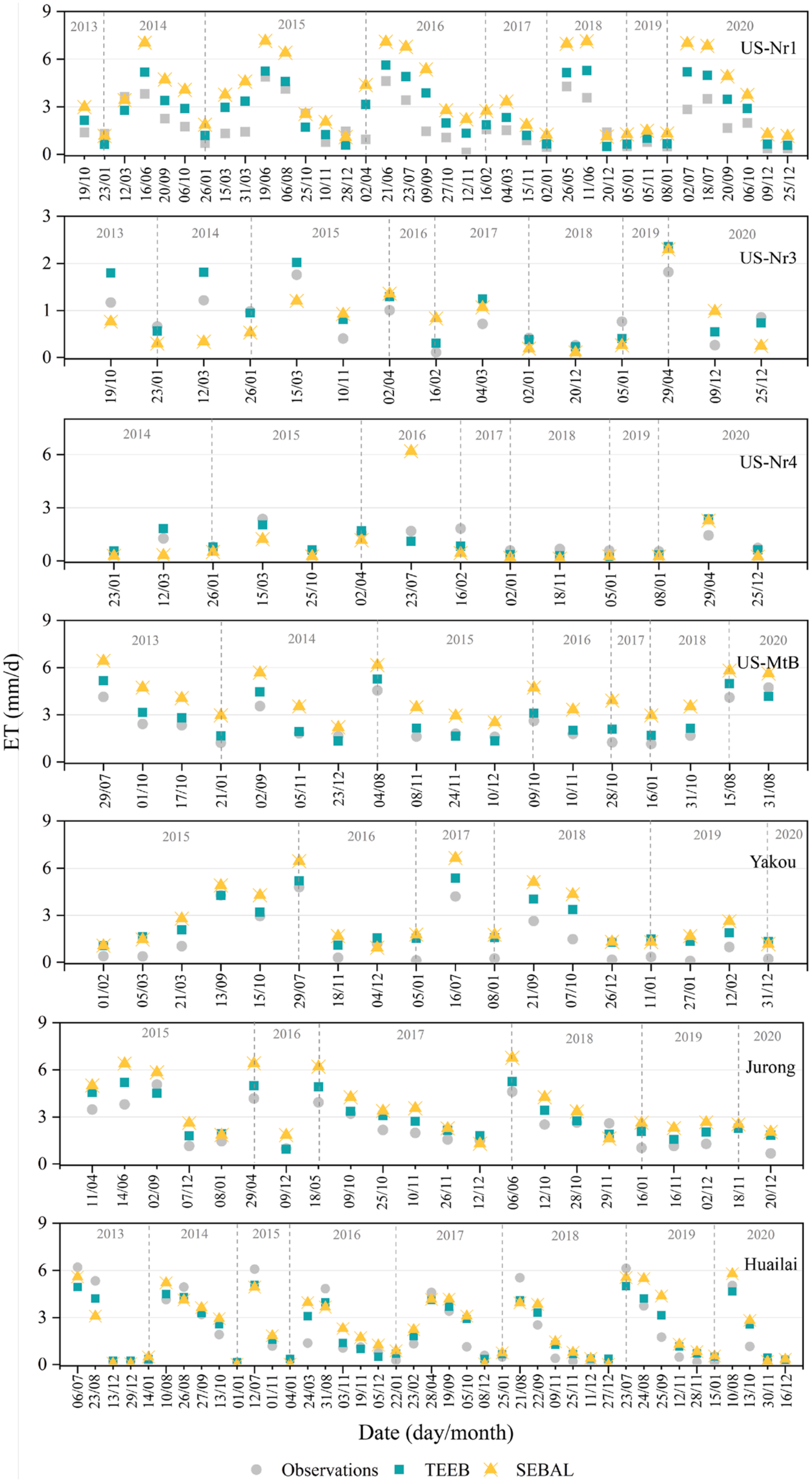

Fig. 6. *ET* comparison between EC flux data and modeled values.

4.3. *Spatial variation in ET simulation*

We further analyzed the simulation results in spatial (Fig. 7). US-MtB (complex terrain) and Huailai (relatively flat areas) were chosen as representatives, and four images over each region were selected. Obviously, *ET* in the warm season was significantly higher than in the cold season owing to factors such as vegetation growth, higher temperature, and radiation (Jung et al., 2010). In terms of spatial distribution, the simulation results of the TEEB model exhibited discrepancies compared to the SEBAL model. The former yielded a more prominent spatial variability, especially over mountainous and sloped areas. It outlined the shape of mountains and demonstrated topographic effects evidently. The latter which, instead, appeared smoother overall.

The comparison of *ET* estimated from the TEEB and SEBAL models at the pixel scale was shown in Fig. 8. It can be seen that the *ET* differences (calculated as TEEB results minus SEBAL results) center around zero,

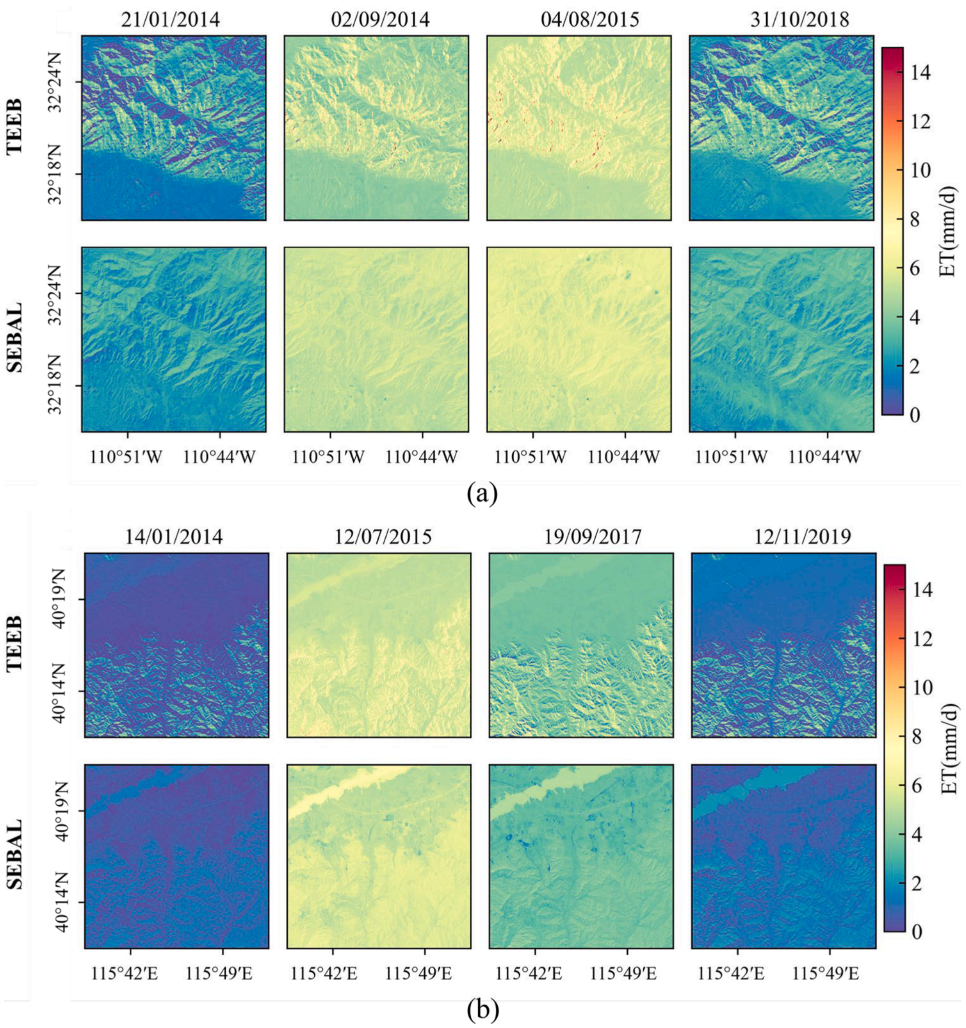

Fig. 7. Spatial distribution of daily *ET* for the selected four days in US-MtB area (21/01/2014, 02/09/2014, 04/08/2015, and 31/10/2018) (a) and Huailai area (14/01/2014, 12/07/2015, 19/09/2017, and 12/11/2019) (b).

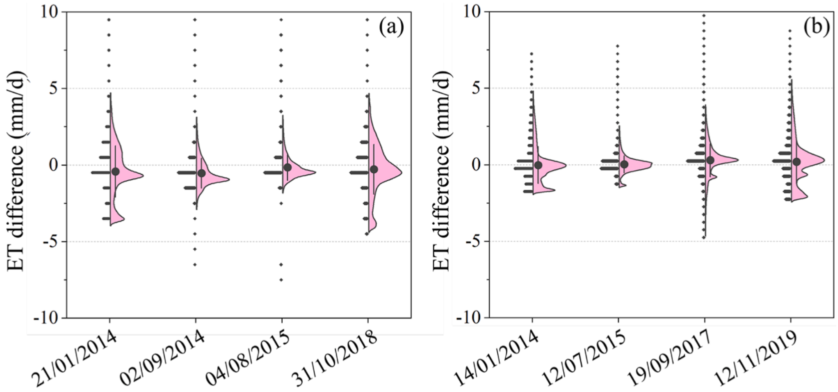

Fig. 8. The difference (TEEB minus SEBAL) in *ET* between the TEEB and SEBAL models for the selected four days over US-MtB area (21/01/2014, 02/09/2014, 04/08/2015, and 31/10/2018) (a) and Huailai area (14/01/2014, 12/07/2015, 19/09/2017, and 12/11/2019) (b). Data are presented on the left and the violin diagram is shown on the right. The 'violin' is a mirror-imaged kernel density plot. The top of the violin diagram is defined as the maximum value; the bottom represents the minimum value; the solid circle in the middle denotes the average value; the upper and lower whiskers indicate the average value ± standard deviation.

indicating that both positive and negative deviations occur (Fig. 8(a)). Compared to the warm season, the *ET* differences in the cold season had a wider spread. In relatively flat areas, the *ET* differences were more narrowly distributed (Fig. 8(b)). Fig. 9 and Fig. 10 showed the *ET* differences on shady and sunlit slopes. From Fig. 9 and Fig. 10, there were partial low values produced by the SEBAL model on sunlit slopes, especially in the cold season. For example, the frequency of *ET* differences greater than zero was higher on 21/01/2014 and 31/10/2018 in the US-MtB area (Fig. 9(a)). This indicated the substantial differences in partitioning of energy fluxes and water vapor fluxes in these areas. In the

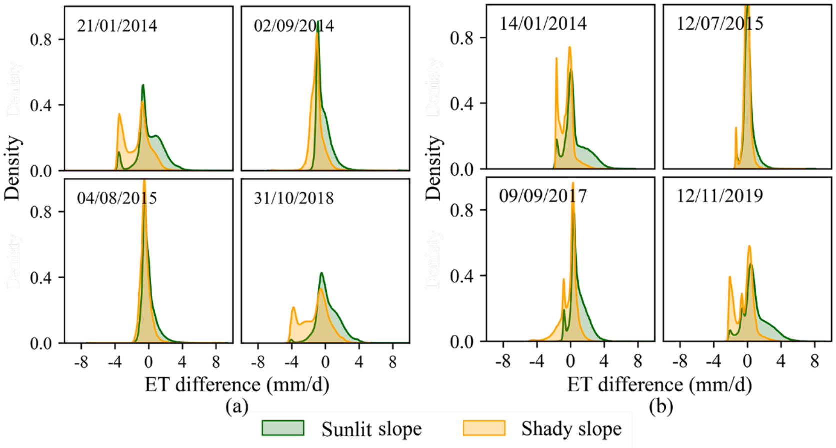

Fig. 9. The density plots of the *ET* difference (TEEB minus SEBAL) estimated using the SEBAL and TEEB models for the selected four days in US-MtB area (21/01/2014, 02/09/2014, 04/08/2015, and 31/10/2018) (a) and Huailai area (14/01/2014, 12/07/2015, 19/09/2017, and 12/11/2019) (b). The same imagery and geographic extents as used in Fig. 7 are used here.

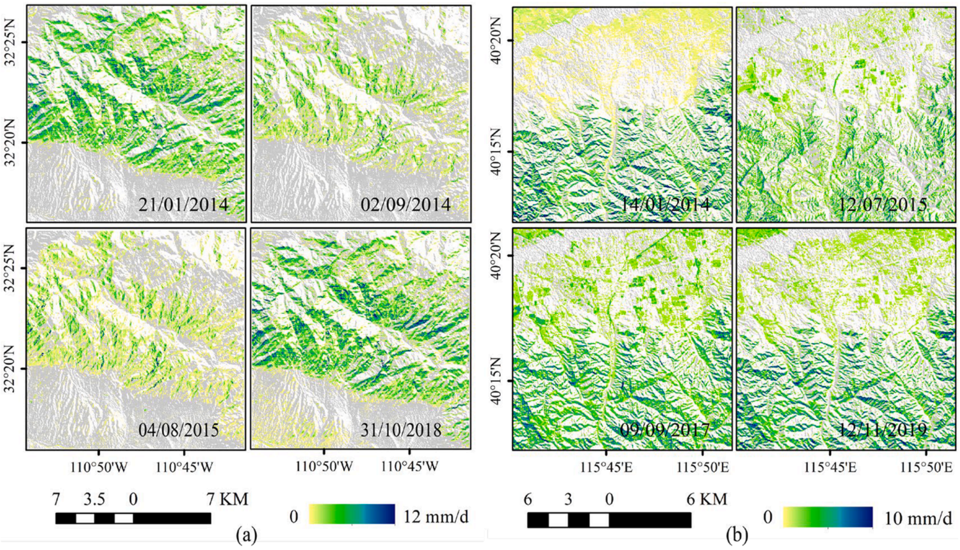

Fig. 10. Spatial pattern of the *ET* difference (TEEB minus SEBAL) for the selected four days in US-MtB area (21/01/2014, 02/09/2014, 04/08/2015, and 31/10/2018) (a) and Huailai area (14/01/2014, 12/07/2015, 19/09/2017, and 12/11/2019) (b). Grey refers to sunlit slope.

SEBAL model, incoming solar radiation ignores aspect leading to the overestimation/underestimation of net radiation on shady/sunlit slopes, respectively, thereby contributing to biases in *ET* estimation. After the autumn equinox, the position of direct solar radiation shifts southward until it reaches the Tropic of Capricorn at the winter solstice. The cold season experienced larger differences in incident angle compared to the warm season, making topographic effects more pronounced in the cold season. Thus, the difference between the TEEB and SEBAL models was greater in the cold season than in the warm season.

4.4. The impact of the topographic effects on ET

The *ET* simulated from the TEEB model varied markedly with topographic factors, following a pattern similar to that of net radiation (Figs. 11–13). This indicated that net radiation was the main energy source of the *ET* and contributed significantly to it (Chen et al., 2013). The result was consistent with the findings of Wang et al. (2022). In terms of slope (Fig. 11), *ET* increased with the increase of slope gradient. This phenomenon was more pronounced in the warm season, especially around the time of the summer solstice. The reason for this result might be the presence of sunshine duration and solar radiation. During the summer solstice, the solar elevation angle reached its maximum, and the slope of the sunny slope was mostly less than or equal to the latitude. Therefore, the sunshine duration on sunlit slopes was long and a slight increase in solar radiation followed the slope. In addition to slope, *ET* was strongly influenced by aspect (Fig. 12). There were prominent differences between sunlit and shady slopes, with *ET* being greater on sunlit than on shady slopes. In comparison with the SEBAL model, the *ET* results estimated by the TEEB model decreased by about 46 % on shady slopes (Fig. 12). As shown in Fig. 12, *ET* on shady slopes was not apparently low in the warm season because the shady slope received substantial sunshine. In the warm season, especially as the summer solstice approached, the sunrise azimuth was nearest to the northeast and the sun set azimuth was nearest to the northwest, and thus the sunshine duration received on shady slopes was not short. Moreover, there was no direct relationship between *ET* estimates and elevation (Fig. 13).

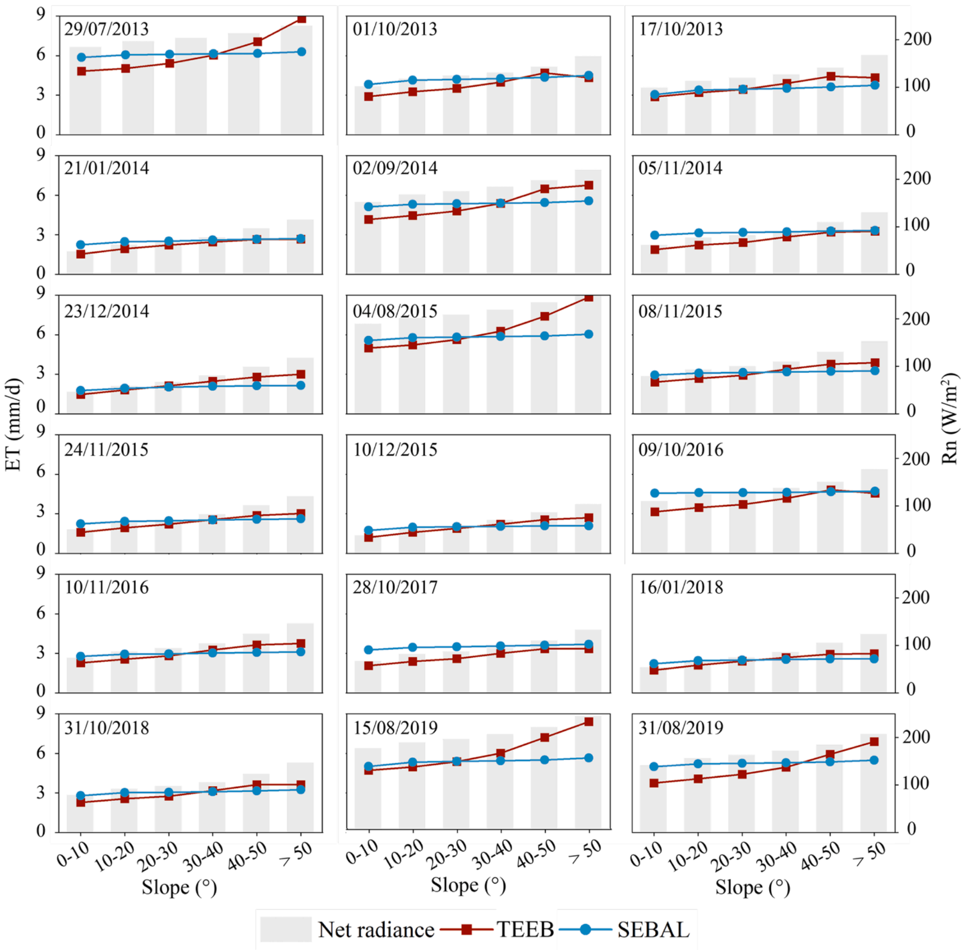

Fig. 11. The *ET* response to slope. The dates above each sub-part refer to the date of image acquisition.

5. Discussion

5.1. Relative contributions of the topographic factors

In mountainous areas, the distribution of surface energy fluxes is significantly affected due to the substantial differences in radiation availability caused by the changes in terrain angle, elevation, and shading (Gao et al., 2008). As Shang et al. (2021) and Gisolo et al. (2022) mentioned that the variability of *ET* was largely related to topography. The SEBAL model misinterprets the temperature difference between shady and sunlit slopes because of its confusion concerning slope and aspect (Bastiaanssen et al., 1998;Liu et al., 2008). This results in the overestimation of *ET*, especially on shady slopes (Figs. 8 and 9).

The relative errors of *ET* provided by the TEEB and SEBAL models in various aspects ranged from −87 % to 86 %. Compared to sunlit slopes, the relative errors were more pronounced on shady slopes (Fig. 14). Specifically, *ET* decreased by about 3–87 % on shady slopes, with the largest changes occurring at aspects from 0 to 45° and from 315° to 360°. It is attributed to the influence of topography on incoming solar radiation (Oliphant et al., 2003;Yang et al., 2019). In mountainous terrain, solar radiation varied strongly with the complex topography (Chow et al., 2013). Shady slopes received lower solar radiation compared to sunlit slopes, which consequently affected *ET*. Nevertheless, this effect was not consistent on sunlit slopes, in particular for aspects from 135° to 225°. In the warm season, *ET* decreased by 5–14 %, while it increased by 2–86 % in the cold season (Fig. 14).

From Figs. 15 and 16, the differences in *ET* estimated by the SEBAL model for various topographic conditions were unremarkable. In contrast, there was a notable spatial heterogeneity in *ET* derived from the TEEB model across different aspects, slopes and elevations. *ET* dramatically increased with slope for aspects from 45° to 315°. In the warm season, the degree to which *ET* increased for aspects from 225° to 315° was greater than the others, varying from 4.244 mm/d to 8.524 mm/d. Similarly, the largest change in the cold season was observed for aspects between 135° and 225° (ranging from 1.866 mm/d to 6.099 mm/d). It was worth noting that *ET* decreased with slope for aspects from 0 to 45° and from 315° to 360°. Particularly, *ET* obtained from the TEEB model was lower and even reached zero at slopes over 50°, which in relation to net radiation (Gao et al., 2008) and solar radiation variations across aspects. In the warm season, solar radiation on sunny slopes increased slightly with increased slope within a certain range, whereas shady slopes showed the opposite trend, though the differences were relatively small. However, these differences were noticeable in the cold season, and the steeper the slope, the greater the discrepancies. As for the elevation, there was no direct relationship between *ET* and elevation for aspects from 0 to 45° and from 315° to 360°. However, *ET* generally tended to decrease at higher elevations for aspects between 45° and 315°. Gao et al. (2008) reported that deficiency in soil moisture and daily net radiation presumably being one of the influence factors.

All in all, it was clear that topographic factors had a significant influence on *ET* estimates in complex terrain. Aspect played a critical role in determining *ET* magnitude and trends. Additionally, the *ET* variation appeared to be more sensitive to slope than elevation.

In order to further explore the impact of topography on *ET* estimates in mountains, we also constructed the model neglecting topography (i.e., the FLAT model). The traditional direct estimation method was adopted to estimate NSR and all parameters in the random forest model were set as default values. The comparison of *ET* obtained from the TEEB

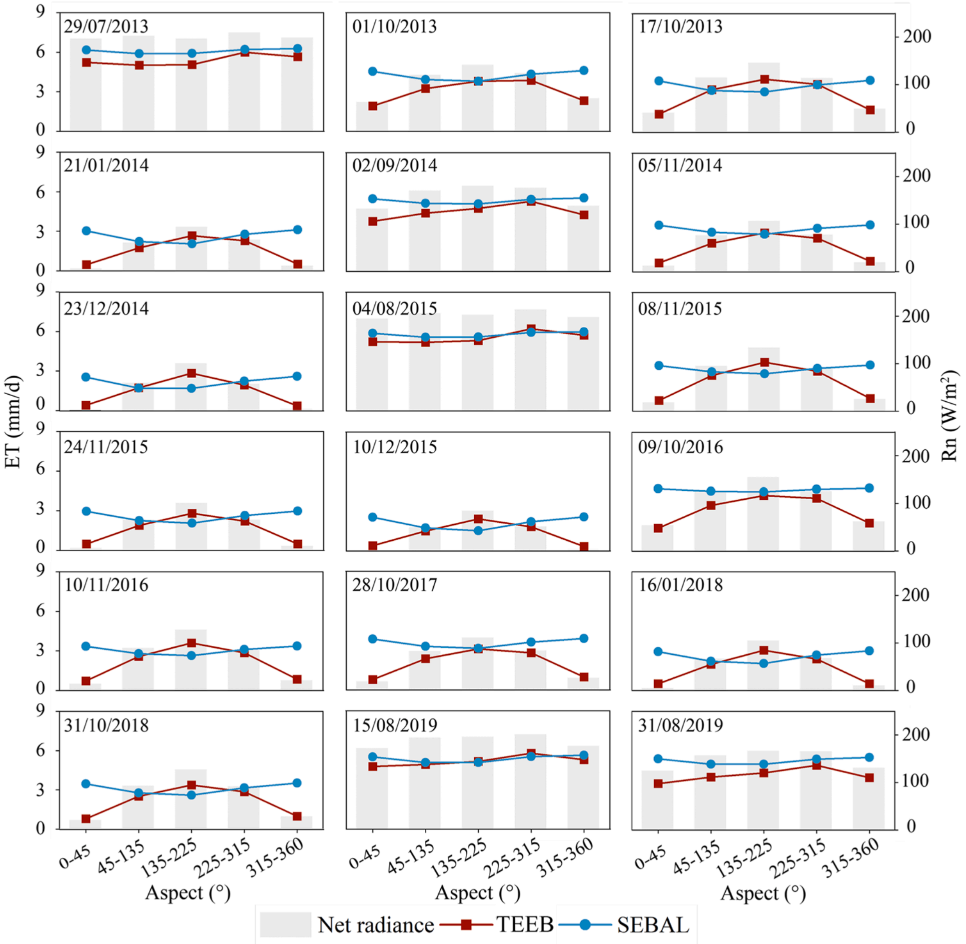

Fig. 12. The *ET* response to aspect. The dates above each sub-part refer to the date of image acquisition.

and FLAT models implied that the average difference (calculated as FLAT results minus TEEB results) in *ET* from the two models ranged from −0.388 mm/d to 0.621 mm/d (see Fig. S1 in the supplementary material). Ignoring topographic effects could produce large errors in *ET* estimates, varying from −11 % to 24 % (see Fig. S2 in the supplementary material).

5.2. Primary uncertainties

Although the TEEB model effectively captures *ET* in complex terrain, uncertainties remain in the *ET* estimates. The uncertainties comprise two primary parts: data sources and models. For data sources, it has been shown that the relative error of vegetation parameters derived from satellite observations is 15–30 % (Wang and Dickinson, 2012) and land surface temperature obtained from remote sensing has the precision accuracy of 2 K (Khan et al., 2021;Li et al., 2015). Similarly, Vanella et al. (2022) identified significant biases in the ERA5 air temperature dataset compared to measurements, the percent bias values were −2 %, 3 % and 4 % under dry and hot-summer temperature climate, hot summer temperature climate conditions and arid, steppe, cold climate conditions, respectively. As the basic and key input parameter for mountainous *ET* estimation, the effects of DEM errors on *ET* cannot be neglected as well (Ma et al., 2022). In order to match the ERA5 dataset to Landsat 8 and DEM data, resampling was performed, which may produce errors.

While EC is widely used for *ET* estimation and is regarded as one of the best available methods, the approach is subject to limitations that can lead to surface energy imbalance. Cause of EC closure problems may be grouped into four broad categories (Volk et al., 2024): instrument error, data processing error, unaccounted energy sources, and sub-mesoscale transport/secondary circulations. The error or uncertainty of EC measurements is approximately 10–30 % based on a comparison of multiple towers at the same site (Mu et al., 2011). In this study, we analyzed energy balance closure and the uncertainty range at the 95 % confidence level at all selected sites in the supplementary material (Table S2). We found a daily closure error of about 41 %, most other studies involving AmeriFlux data report closure errors between 20 % and 30 % (Eshonkulov et al., 2019;Stoy et al., 2013;Wilson et al., 2002). After energy closure correction based on the Bowen ratio method (Twine et al., 2000), the average closure error was reduced to 7 %. We acknowledge that the EC measurements still have uncertainties and other errors that are difficult or currently impossible to account for. Yet, the EC measurements used for comparison provide a consistent and reproducible benchmark for evaluating the *ET* estimates from all models.

The simple square 'static' pixel (Landsat 30 m) grid of 3 × 3 drawn around site locations was used as flux tower source area in this study. However, the EC measurements typically represent a scale of several hundred meters (Li et al., 2008), which may lead to the uncertainty of *ET* estimation (Yao et al., 2014). The TEEB model, same as the SEBAL model, does not distinguish vegetation and soil. This may lead to discrepancies between the estimated and actual values. Furthermore, the model employed a constant evaporation fraction to extend instantaneous latent heat flux to daily *ET*. In reality, the evaporation fraction varies throughout the day, these also bring large uncertainties in *ET* modeling.

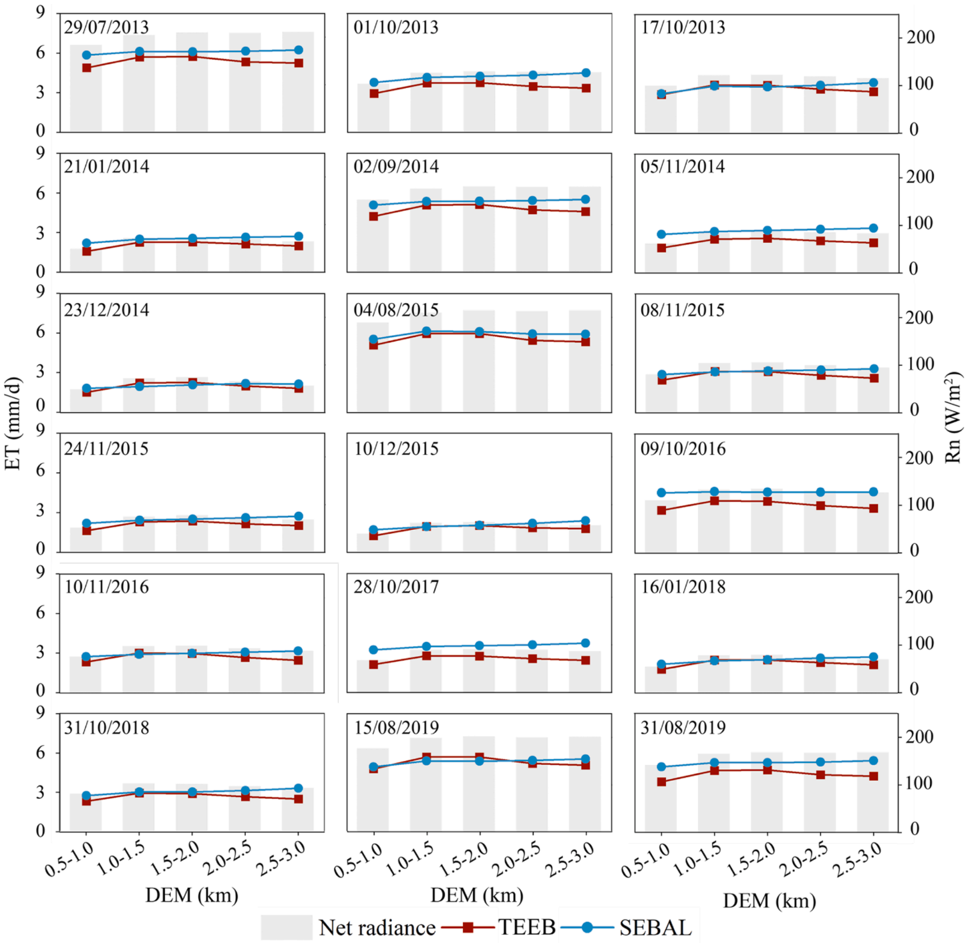

Fig. 13. The *ET* response to DEM. The dates above each sub-part refer to the date of image acquisition.

5.3. Advantages and limitations

The TEEB model, which incorporates the topographic effects on net radiation, was developed to estimate *ET* in mountainous regions. The model achieved satisfactory performance in both complex terrain (US-Nr1, US-Nr3, US-Nr4, US-MtB, and Yakou) (average RMSE=0.504 mm/d) and relatively flat areas (Jurong and Huailai) (average RMSE=0.551 mm/d), indicating its robustness and stability (Table 2, Figs. 6 and 7). Compared to the SEBAL model, it effectively reduced estimation errors and extended the applicability of SEBAL to mountainous terrain, further highlighting the superiority of the TEEB model for estimating *ET* over mountainous terrain (Figs. 3–5,7).

However, the model we constructed incorporates only the influence of topography on shortwave radiation. Longwave radiation and other key parameters (e.g., surface albedo, air temperature, and surface temperature) in *ET* estimation are also affected by topographic effects. Future studies can aim to enhance the capability of the TEEB model by fully considering the impact of topographic factors on key parameters in *ET* estimation, enabling high spatial resolution *ET* monitoring under complex terrain.

6. Conclusion

This study developed a terrain-extended *ET* model, the TEEB model, which takes into account topographic effects to realize the *ET* method applicable to mountainous terrain. The proposed TEEB model was evaluated over seven eddy covariance towers. The performance of the TEEB model was also assessed against the most widely used SEBAL model.

The TEEB model performed well against EC measurement data in mountainous areas, with a RMSE of 0.713 mm/d, an R^2 of 0.798, and a MAE of 0.571 mm/d. Compared to the SEBAL model, the TEEB model significantly enhanced the accuracy of *ET* estimation, reducing RMSE and MAE by approximately 42 % and increasing R^2 by about 2 %. The performance of the TEEB model in complex terrain (average RMSE=0.504 mm/d) was comparable to that in relatively flat areas (average RMSE=0.551 mm/d), indicating its stability and robustness. In terms of spatial distribution, the simulation results of the TEEB model exhibited distinct topographic characteristics. Moreover, *ET* estimates would be reduced by 46 % on shady slopes with a proper consideration of topographic effects. The analysis of the relative contributions of the topographic factors confirmed their importance for *ET* estimation in complex terrain (aspect played a critical role in determining *ET* magnitude and trends; the *ET* variation appeared to be more sensitive to slope than elevation). Ignoring topographic effects could lead to a relative error in *ET* estimation of −11–24 %. In conclusion, consideration of topographic effects is necessary when estimating *ET* in mountainous areas. The proposed model achieves the *ET* estimation over mountainous terrain. This study deepens our understanding of regional energy exchange processes and offers a potential solution to the global surface energy imbalance. It contributes to the study and management of regional climate, water resources, and ecosystems, promoting sustainable development in mountainous areas.

Code availability

The code used to estimate NSR in mountains used in this study is publicly available from https://doi.org/10.6084/m9.figshare.2811408

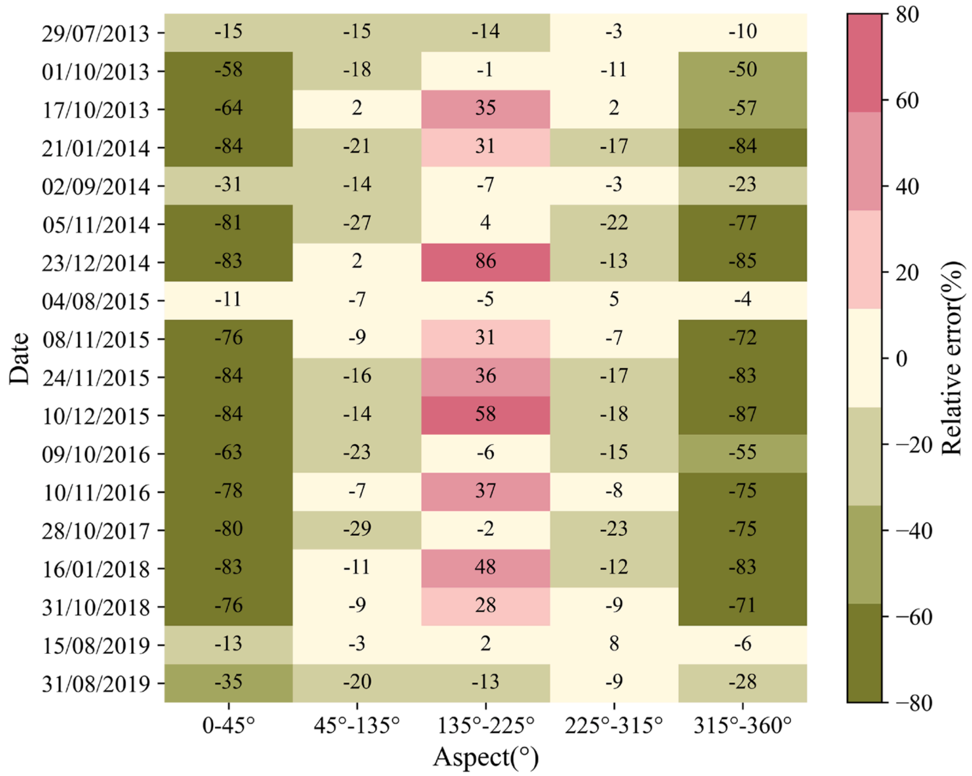

Fig. 14. The relative errors ($RE = \frac{ET_{TEEB} - ET_{SEBAL}}{ET_{SEBAL}} \times 100$) of *ET* derived from the TEEB and SEBAL models.

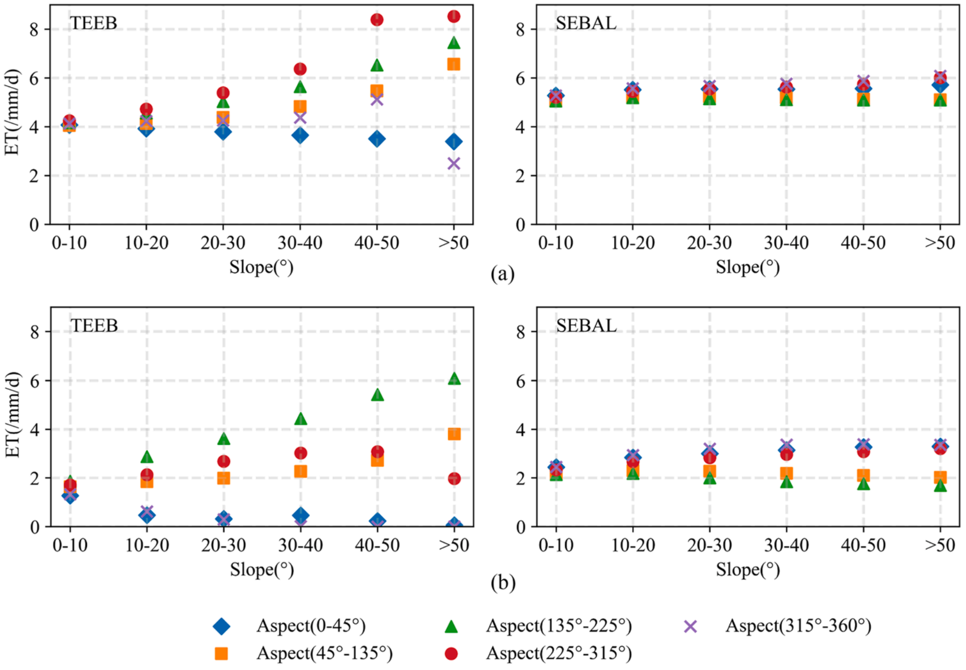

Fig. 15. The *ET* response to slope for different aspects on 02/09/2014 (a) and 16/01/2018 (b).

5.v1.

CRediT authorship contribution statement

Yixiao Zhang: Writing – original draft, Visualization, Methodology, Formal analysis, Data curation, Conceptualization. **Tao He:** Writing – review & editing, Methodology, Supervision, Funding acquisition, Conceptualization. **Shunlin Liang:** Writing – review & editing, Supervision. **Yichuan Ma:** Writing – review & editing, Methodology. **Yunjun Yao:** Writing – review & editing.

Declaration of competing interest

The authors declare that they have no known competing financial

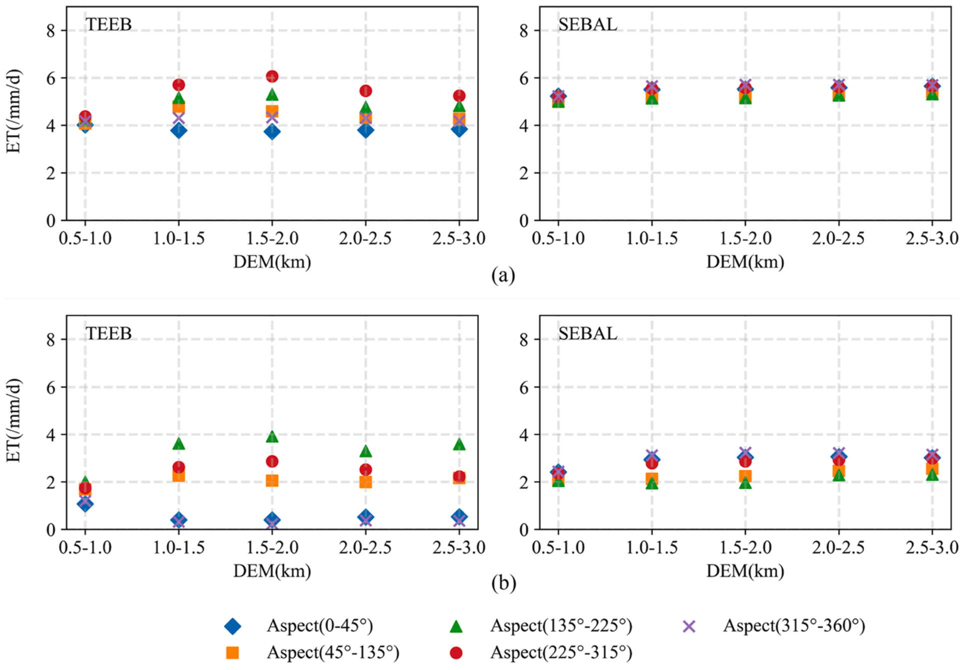

Fig. 16. The *ET* response to elevation for different aspects on 02/09/2014 (a) and 16/01/2018 (b).

interests or personal relationships that could have appeared to influence the work reported in this paper.

Acknowledgments

This research is supported by the National Science Foundation of China Grant (42090012), the National Natural Science Foundation of China (42271404), the Advanced Research Project: Remote sensing inversion of key land surface elements and development of quantitative products, the Open Fund of Key Laboratory of National Geographical Census and Monitoring, Ministry of Natural Resources of China (2025NGCM01), the National Key Research and Development Program of China (2020YFA0608704), the Fundamental Research Funds for the Central Universities through Wuhan University (2042022dx001). We thank all the accessible datasets used in this paper provided by USGS, JAXA, NASA, AmeriFlux, the National Tibetan Plateau Data Center, and the National Ecosystem Science Data Center. We especially thank Zhongguo Zhao's help in processing the data and writing the manuscript. Finally, we greatly appreciate editor and anonymous reviewers for their valuable comments which substantially improved the manuscript.

Supplementary materials

Supplementary material associated with this article can be found, in the online version, at doi:10.1016/j.agrformet.2025.110468.

Data availability

Data will be made available on request.

References

Aguilar, C., Herrero, J., Polo, M., 2010. Topographic effects on solar radiation distribution in mountainous watersheds and their influence on reference evapotranspiration estimates at watershed scale. Hydrol. Earth Syst. Sci. 14 (12), 2479–2494.

Allen, R.G., Tasumi, M., Trezza, R., 2007. Satellite-based energy balance for mapping evapotranspiration with internalized calibration (METRIC)—Model. J. Irrig. Drain. Eng. 133 (4), 380–394.

Allen, R.G., Trezza, R., Tasumi, M., 2006. Analytical integrated functions for daily solar radiation on slopes. Agric. For. Meteorol. 139 (1–2), 55–73.

Anderson, M.C., Allen, R.G., Morse, A., Kustas, W.P., 2012. Use of Landsat thermal imagery in monitoring evapotranspiration and managing water resources. Remote Sens. Environ. 122, 50–65.

Baldridge, A.M., Hook, S.J., Grove, C., Rivera, G., 2009. The ASTER spectral library version 2.0. Remote Sens. Environ. 113 (4), 711–715.

Barsi, J.A., Lee, K., Kvaran, G., Markham, B.L., Pedelty, J.A., 2014. The spectral response of the Landsat-8 operational land imager. Remote Sens. Appl.: Soc. Environ. 6 (10), 10232–10251.

Barzkar, A., Shahabi, S., Niazmradi, S., Madadi, M.R., 2021. A comparative study of remote sensing and gene expression programming for estimation of evapotranspiration in four distinctive climates. Stochastic Environ. Res. Risk Assess. 35 (7), 1437–1452.

Bastiaanssen, W.G., Menenti, M., Feddes, R., Holtslag, A., 1998. A remote sensing surface energy balance algorithm for land (SEBAL). 1. Formulation. J. Hydrol. 212, 198–212.

Bastiaanssen, W.G.M., 2000. SEBAL-based sensible and latent heat fluxes in the irrigated Gediz Basin. Turkey. J. Hydrol. 229 (1–2), 87–100.

Beniston, M., Stoffel, M., 2014. Assessing the impacts of climatic change on mountain water resources. Sci. Total Environ. 493, 1129–1137.

Briner, S., Huber, R., Bebi, P., Elkin, C., Schmatz, D.R., Grêt-Regamey, A., 2013. Trade-offs between ecosystem services in a mountain region. Ecol. Soc. 18 (3).

Burns, S.P., Blanken, P.D., Turnipseed, A.A., Hu, J., Monson, R.K., 2015. The influence of warm-season precipitation on the diel cycle of the surface energy balance and carbon dioxide at a Colorado subalpine forest site. Biogeosciences 12 (23), 7349–7377.

Carrera-Hernandez, J., 2021. Not all DEMs are equal: an evaluation of six globally available 30 m resolution DEMs with geodetic benchmarks and LiDAR in Mexico. Remote Sens. Environ. 261, 112474.

Carter, C., Liang, S., 2019. Evaluation of ten machine learning methods for estimating terrestrial evapotranspiration from remote sensing. Int. J. Appl. Earth Obs. Geoinf. 78, 86–92.

Castelli, M., Anderson, M., Yang, Y., Wohlfahrt, G., Bertoldi, G., Niedrist, G., Hammerle, A., Zhao, P., Zebisch, M., Notarnicola, C., 2018. Two-source energy balance modeling of evapotranspiration in Alpine grasslands. Remote Sens. Environ. 209, 327–342.

Chander, G., Markham, B.L., Helder, D.L., 2009. Summary of current radiometric calibration coefficients for Landsat MSS, TM, ETM+, and EO-1 ALI sensors. Remote Sens. Environ. 113 (5), 893–903.

Chang, Y., Wang, J., Qin, D., Ding, Y., Zhao, Q., Liu, F., Zhang, S., 2017. Methodological comparison of alpine meadow evapotranspiration on the Tibetan Plateau, China. PLoS One 12 (12), e0189059.

Chen, H., Jeanne Huang, J., Liang, H., Wang, W., Li, H., Wei, Y., Jiang, A.Z., Zhang, P., 2023. Integration of flux footprint and physical mechanism into convolutional neural network model for enhanced simulation of urban evapotranspiration. J. Hydrol. 619, 129016.

Chen, J., He, T., Liang, S., 2022a. Estimation of daily all-wave surface net radiation with multispectral and multitemporal observations from GOES-16 ABI. IEEE Trans. Geosci. Remote Sens. 60, 1–16.

Chen, J., He, T., Liang, S., 2022b. Estimation of daily all-wave surface net radiation with multispectral and multitemporal observations from GOES-16 ABI. IEEE Trans. Geosci. Remote Sens. 60, 1–16.

Chen, X., Su, Z., Ma, Y., Yang, K., Wang, B., 2013. Estimation of surface energy fluxes under complex terrain of Mt. Qomolangma over the Tibetan Plateau. Hydrol. Earth Syst. Sci. 17 (4), 1607–1618.

Chow, F.K., De Wekker, S.F., Snyder, B.J., 2013. Mountain Weather Research and forecasting: Recent Progress and Current Challenges, 750. Springer.

Clark, R.N., Swayze, G.A., Wise, R.A., Livo, K.E., Hoefen, T.M., Kokaly, R.F., Sutley, S.J., 2007. USGS Digital Spectral Library splib06a. 2327-638X,. US Geological Survey.

Douna, V., Barraza, V., Grings, F., Huete, A., Restrepo-Coupe, N., Beringer, J., 2021. Towards a remote sensing data based evapotranspiration estimation in Northern Australia using a simple random forest approach. J. Arid. Environ. 191, 104513.

Ershadi, A., McCabe, M.F., Evans, J.P., Walker, J.P., 2013. Effects of spatial aggregation on the multi-scale estimation of evapotranspiration. Remote Sens. Environ. 131, 51–62.

Eshonkulov, R., Poyda, A., Ingwersen, J., Wizemann, H.-D., Weber, T.K., Kremer, P., Högy, P., Pulatov, A., Streck, T., 2019. Evaluating multi-year, multi-site data on the energy balance closure of eddy-covariance flux measurements at cropland sites in southwestern Germany. Biogeosciences 16 (2), 521–540.

Falge, E., Baldocchi, D., Olson, R., Anthoni, P., Aubinet, M., Bernhofer, C., Burba, G., Ceulemans, R., Clement, R., Dolman, H., 2001a. Gap filling strategies for defensible annual sums of net ecosystem exchange. Agric. For. Meteorol. 107 (1), 43–69.

Falge, E., Baldocchi, D., Olson, R., Anthoni, P., Aubinet, M., Bernhofer, C., Burba, G., Ceulemans, R., Clement, R., Dolman, H., 2001b. Gap filling strategies for long term energy flux data sets. Agric. For. Meteorol. 107 (1), 71–77.

Fisher, J.B., Melton, F., Middleton, E., Hain, C., Anderson, M., Allen, R., McCabe, M.F., Hook, S., Baldocchi, D., Townsend, P.A., 2017. The future of evapotranspiration: global requirements for ecosystem functioning, carbon and climate feedbacks, agricultural management, and water resources. Water Resour. Res. 53 (4), 2618–2626.

Forster, P., Storelvmo, T., Armour, K., Collins, W., Dufresne, J.-L., Frame, D., Lunt, D., Mauritsen, T., Palmer, M., Watanabe, M., 2021. The Earth's energy budget, climate feedbacks, and climate sensitivity. Climate Change 2021: The Physical Science Basis. Contribution of Working Group I to the Sixth Assessment Report of the Intergovernmental Panel on Climate Change.

Gao, Y., Long, D., Li, Z.L., 2008. Estimation of daily actual evapotranspiration from remotely sensed data under complex terrain over the upper Chao river basin in North China. Int. J. Remote Sens. 29 (11), 3295–3315.

Gisolo, D., Previati, M., Bevilacqua, I., Canone, D., Boetti, M., Dematteis, N., Balocco, J., Ferrari, S., Gentile, A., N'Sassila, M., Heery, B., Vereecken, H., Ferraris, S., 2022. A calibration free radiation driven model for estimating actual evapotranspiration of mountain grasslands (CLIME-MG). J. Hydrol. 610, 127948.

Gobiet, A., Kotlarski, S., Beniston, M., Heinrich, G., Rajczak, J., Stoffel, M., 2014. 21st century climate change in the European Alps—a review. Sci. Total Environ. 493, 1138–1151.

Grêt-Regamey, A., Weibel, B., 2020. Global assessment of mountain ecosystem services using earth observation data. Ecosyst. Serv. 46, 101213.

Guo, A., Liu, S., Zhu, Z., Xu, Z., Xiao, Q., Ju, Q., Zhang, Y., Yang, X., 2020. Impact of lake/reservoir expansion and shrinkage on energy and water vapor fluxes in the surrounding area. J. Geophys. Res.: Atmos. 125 (20), e2020JD032833.

Guo, T., He, T., Liang, S., Roujean, J.-L., Zhou, Y., Huang, X., 2022. Multi-decadal analysis of high-resolution albedo changes induced by urbanization over contrasted Chinese cities based on Landsat data. Remote Sens. Environ. 269, 112832.

Hantson, S., Chuvieco, E., 2011. Evaluation of different topographic correction methods for Landsat imagery. Int. J. Appl. Earth Observ. Geoinf. 13 (5), 691–700.

Hoek van Dijke, A.J., Mallick, K., Schlerf, M., Machwitz, M., Herold, M., Teuling, A.J., 2020. Examining the link between vegetation leaf area and land–atmosphere exchange of water, energy, and carbon fluxes using FLUXNET data. Biogeosciences 17 (17), 4443–4457.

Holland, P., Steyn, D., 1975. Vegetational responses to latitudinal variations in slope angle and aspect. J. Biogeogr. 179–183.

Horn, B.K., 1981. Hill shading and the reflectance map. Proc. IEEE 69 (1), 14–47.

Hua, D., Hao, X., Zhang, Y., Qin, J., 2020. Uncertainty assessment of potential evapotranspiration in arid areas, as estimated by the Penman-Monteith method. J. Arid. Land 12, 166–180.

Immerzeel, W.W., Lutz, A.F., Andrade, M., Bahl, A., Biemans, H., Bolch, T., Hyde, S., Brumby, S., Davies, B.J., Elmore, A.C., Emmer, A., Feng, M., Fernández, A., Haritashya, U., Kargel, J.S., Koppes, M., Kraaijenbrink, P.D.A., Kulkarni, A.V., Mayewski, P.A., Nepal, S., Pacheco, P., Painter, T.H., Pellicciotti, F., Rajaram, H., Rupper, S., Sinisalo, A., Shrestha, A.B., Viviroli, D., Wada, Y., Xiao, C., Yao, T., Baillie, J.E.M., 2020. Importance and vulnerability of the world's water towers. Nature 577 (7790), 364–369.

Immerzeel, W.W., van Beek, L.P.H., Bierkens, M.F.P., 2010. Climate change will affect the Asian water towers. Science 328 (5984), 1382–1385.

Jackson, R.D., Reginato, R., Idso, S., 1977. Wheat canopy temperature: a practical tool for evaluating water requirements. Water Resour. Res. 13 (3), 651–656.

Jia, Z., Liu, S., Xu, Z., Chen, Y., Zhu, M., 2012. Validation of remotely sensed evapotranspiration over the Hai River Basin, China. J. Geophys. Res.: Atmos. 117 (D13).

Jung, M., Reichstein, M., Ciais, P., Seneviratne, S.I., Sheffield, J., Goulden, M.L., Bonan, G., Cescatti, A., Chen, J., de Jeu, R., Dolman, A.J., Eugster, W., Gerten, D., Gianelle, D., Gobron, N., Heinke, J., Kimball, J., Law, B.E., Montagnani, L., Mu, Q., Mueller, B., Oleson, K., Papale, D., Richardson, A.D., Roupsard, O., Running, S., Tomelleri, E., Viovy, N., Weber, U., Williams, C., Wood, E., Zaehle, S., Zhang, K., 2010. Recent decline in the global land evapotranspiration trend due to limited moisture supply. Nature 467 (7318), 951–954.

Khan, M.S., Jeong, J., Choi, M., 2021. An improved remote sensing based approach for predicting actual evapotranspiration by integrating LiDAR. Adv. Space Res. 68 (4), 1732–1753.

Kim, H.-Y., Liang, S., 2010. Development of a hybrid method for estimating land surface shortwave net radiation from MODIS data. Remote Sens. Environ. 114 (11), 2393–2402.

Knowles, J.F., Blanken, P.D., Williams, M.W., Chowanski, K.M., 2012. Energy and surface moisture seasonally limit evaporation and sublimation from snow-free alpine tundra. Agric. For. Meteorol. 157, 106–115.

Knowles, J.F., Scott, R.L., Minor, R.L., Barron-Gafford, G.A., 2020. Ecosystem carbon and water cycling from a sky island montane forest. Agric. For. Meteorol. 281, 107835.

Li, F., Jupp, D.L., Reddy, S., Lymburner, L., Mueller, N., Tan, P., Islam, A., 2010. An evaluation of the use of atmospheric and BRDF correction to standardize Landsat data. IEEE J. Selected Topics Appl. Earth Observ. Remote Sens. 3 (3), 257–270.

Li, F., Jupp, D.L., Thankappan, M., Lymburner, L., Mueller, N., Lewis, A., Held, A., 2012. A physics-based atmospheric and BRDF correction for Landsat data over mountainous terrain. Remote Sens. Environ. 124, 756–770.

Li, F., Kustas, W.P., Anderson, M.C., Prueger, J.H., Scott, R.L., 2008. Effect of remote sensing spatial resolution on interpreting tower-based flux observations. Remote Sens. Environ. 112 (2), 337–349.

Li, Y., Wang, W., Wang, G., Tan, Q., 2022. Actual evapotranspiration estimation over the Tuojiang River Basin based on a hybrid CNN-RF model. J. Hydrol. 610, 127788.

Li, Y., Zhou, J., Wang, H., Li, D., Jin, R., Zhou, Y., Zhou, Q., 2015. Integrating soil moisture retrieved from L-band microwave radiation into an energy balance model to improve evapotranspiration estimation on the irrigated oases of arid regions in northwest China. Agricult. Forest Meteorol. 214, 306–318.

Liang, S., Strahler, A.H., Walthall, C., 1999. Retrieval of land surface albedo from satellite observations: a simulation study. J. Appl. Meteorol. 38 (6), 712–725.

Liu, C., Gao, W., Gao, Z., Xu, S., 2008. Improvements of Regional Evapotranspiration Model by Considering Topography Correction. Remote Sensing and Modeling of Ecosystems for Sustainability V. SPIE, pp. 120–126.

Liu, S., Li, X., Xu, Z., Che, T., Xiao, Q., Ma, M., Liu, Q., Jin, R., Guo, J., Wang, L., 2018a. The Heihe Integrated Observatory Network: a basin-scale land surface processes observatory in China. Vadose Zone J. 17 (1), 1–21.

Liu, W., Sun, F., Li, Y., Zhang, G., Sang, Y.-F., Lim, W.H., Liu, J., Wang, H., Bai, P., 2018b. Investigating water budget dynamics in 18 river basins across the Tibetan Plateau through multiple datasets. Hydrol. Earth Syst. Sci. 22 (1), 351–371.

Long, D., Singh, V.P., 2012. A two-source trapezoid model for evapotranspiration (TTME) from satellite imagery. Remote Sens. Environ. 121, 370–388.

Ma, Y., He, T., Liang, S., McVicar, T.R., Hao, D., Liu, T., Jiang, B., 2023a. Estimation of fine spatial resolution all-sky surface net shortwave radiation over mountainous terrain from Landsat 8 and Sentinel-2 data. Remote Sens. Environ. 285, 113364.

Ma, Y., He, T., Liang, S., Xiao, X., 2022. Quantifying the impacts of DEM uncertainty on clear-sky surface shortwave radiation estimation in typical mountainous areas. Agric. For. Meteorol. 327, 109222.

Ma, Y., Sun, S., Li, C., Zhao, J., Li, Z., Jia, C., 2023b. Estimation of regional actual evapotranspiration based on the improved SEBAL model. J. Hydrol. 619, 129283.

Mayer, B., Kylling, A., 2005. The libRadtran software package for radiative transfer calculations-description and examples of use. Atmosph. Chem. Phys. 5 (7), 1855–1877.

McVicar, T.R., Van Niel, T.G., Li, L., Hutchinson, M.F., Mu, X., Liu, Z., 2007. Spatially distributing monthly reference evapotranspiration and pan evaporation considering topographic influences. J. Hydrol. 338 (3–4), 196–220.

Mu, Q., Zhao, M., Running, S.W., 2011. Improvements to a MODIS global terrestrial evapotranspiration algorithm. Remote Sens. Environ. 115 (8), 1781–1800.

Muñoz-Sabater, J., Dutra, E., Agustí-Panareda, A., Albergel, C., Arduini, G., Balsamo, G., Boussetta, S., Choulga, M., Harrigan, S., Hersbach, H., Martens, B., Miralles, D.G., Piles, M., Rodríguez-Fernández, N.J., Zsoter, E., Buontempo, C., Thépaut, J.N., 2021. ERA5-Land: a state-of-the-art global reanalysis dataset for land applications. Earth Syst. Sci. Data 13 (9), 4349–4383.

Norman, J.M., Kustas, W.P., Humes, K.S., 1995. Source approach for estimating soil and vegetation energy fluxes in observations of directional radiometric surface temperature. Agric. For. Meteorol. 77 (3), 263–293.

Nyambayo, V.P., Potts, D.M., 2010. Numerical simulation of evapotranspiration using a root water uptake model. Comput. Geotech. 37 (1), 175–186.

Oliphant, A.J., Spronken-Smith, R.A., Sturman, A.P., Owens, I.F., 2003. Spatial variability of surface radiation fluxes in mountainous terrain. J. Appl. Meteorol. 42 (1), 113–128.

Pedregosa, F., Varoquaux, G., Gramfort, A., Michel, V., Thirion, B., Grisel, O., Blondel, M., Prettenhofer, P., Weiss, R., Dubourg, V., 2011. Scikit-learn: machine learning in Python. J. Mach. Learn. Res. 12, 2825–2830.

Pütz, T., Kiese, R., Wollschläger, U., Groh, J., Rupp, H., Zacharias, S., Priesack, E., Gerke, H., Gasche, R., Bens, O., 2016. TERENO-SOILCan: a lysimeter-network in Germany observing soil processes and plant diversity influenced by climate change. Environ. Earth Sci. 75, 1–14.

Rahimzadegan, M., Janani, A., 2019. Estimating evapotranspiration of pistachio crop based on SEBAL algorithm using Landsat 8 satellite imagery. Agric. Water Manage. 217, 383–390.

Sandmeier, S., Itten, K.I., 1997. A physically-based model to correct atmospheric and illumination effects in optical satellite data of rugged terrain. IEEE Trans. Geosci. Remote Sens. 35 (3), 708–717.

Shang, K., Yao, Y., Liang, S., Zhang, Y., Fisher, J.B., Chen, J., Liu, S., Xu, Z., Zhang, Y., Jia, K., Zhang, X., Yang, J., Bei, X., Guo, X., Yu, R., Xie, Z., Zhang, L., 2021. DNN-MET: a deep neural networks method to integrate satellite-derived evapotranspiration products, eddy covariance observations and ancillary information. Agric. For. Meteorol. 308–309.

Shuttleworth, W., Gurney, R., Hsu, A., Ormsby, J., 1989. FIFE: The variation in Energy Partition at Surface Flux Sites, 186. IAHS Publ, pp. 523–534.

Stoy, P.C., Mauder, M., Foken, T., Marcolla, B., Boegh, E., Ibrom, A., Arain, M.A., Arneth, A., Aurela, M., Bernhofer, C., Cescatti, A., Dellwik, E., Duce, P., Gianelle, D., van Gorsel, E., Kiely, G., Knohl, A., Margolis, H., McCaughey, H., Merbold, L., Montagnani, L., Papale, D., Reichstein, M., Saunders, M., Serrano-Ortiz, P., Sottocornola, M., Spano, D., Vaccari, F., Varlagin, A., 2013. A data-driven analysis of energy balance closure across FLUXNET research sites: the role of landscape scale heterogeneity. Agric. For. Meteorol. 171-172, 137–152. https://doi.org/10.1016/j.agrformet.2012.11.004.

Su, Z., 2002. The surface energy balance system (SEBS) for estimation of turbulent heat fluxes. Hydrol. Earth Syst. Sci. 6 (1), 85–100.

Tang, R., Li, Z.-L., Chen, K.-S., Jia, Y., Li, C., Sun, X., 2013. Spatial-scale effect on the SEBAL model for evapotranspiration estimation using remote sensing data. Agric. For. Meteorol. 174, 28–42.

Taylor, K.E., 2001. Summarizing multiple aspects of model performance in a single diagram. J. Geophys. Res.: Atmos. 106 (D7), 7183–7192.

Twine, T.E., Kustas, W., Norman, J., Cook, D., Houser, P., Meyers, T., Prueger, J., Starks, P., Wesely, M., 2000. Correcting eddy-covariance flux underestimates over a grassland. Agric. For. Meteorol. 103 (3), 279–300.

Vanella, D., Longo-Minnolo, G., Belfiore, O.R., Ramírez-Cuesta, J.M., Pappalardo, S., Consoli, S., D'Urso, G., Chirico, G.B., Coppola, A., Comegna, A., 2022. Comparing the use of ERA5 reanalysis dataset and ground-based agrometeorological data under different climates and topography in Italy. J. Hydrol.: Reg. Stud. 42, 101182.

Viviroli, D., Dürr, H.H., Messerli, B., Meybeck, M., Weingartner, R., 2007. Mountains of the world, water towers for humanity: typology, mapping, and global significance. Water Resour. Res 43 (7).

Volk, J.M., Huntington, J.L., Melton, F.S., Allen, R., Anderson, M., Fisher, J.B., Kilic, A., Ruhoff, A., Senay, G.B., Minor, B., 2024. Assessing the accuracy of OpenET satellite-based evapotranspiration data to support water resource and land management applications. Nat. Water 2 (2), 193–205.

Wang, K., Dickinson, R.E., 2012. A review of global terrestrial evapotranspiration: observation, modeling, climatology, and climatic variability. Rev. Geophys. 50 (2).

Wang, L., Wu, B., Elnashar, A., Zhu, W., Yan, N., Ma, Z., Liu, S., Niu, X., 2022. Incorporation of net radiation model considering complex terrain in evapotranspiration determination with sentinel-2 data. Remote Sens. 14 (5).

Wang, T., Yan, G., Mu, X., Jiao, Z., Chen, L., Chu, Q., 2018. Toward operational shortwave radiation modeling and retrieval over rugged terrain. Remote Sens. Environ. 205, 419–433.

Wilson, K., Goldstein, A., Falge, E., Aubinet, M., Baldocchi, D., Berbigier, P., Bernhofer, C., Ceulemans, R., Dolman, H., Field, C., 2002. Energy balance closure at FLUXNET sites. Agric. For. Meteorol. 113 (1–4), 223–243.

Wulder, M.A., Loveland, T.R., Roy, D.P., Crawford, C.J., Masek, J.G., Woodcock, C.E., Allen, R.G., Anderson, M.C., Belward, A.S., Cohen, W.B., 2019. Current status of Landsat program, science, and applications. Remote Sens. Environ. 225, 127–147.

Xu, T., Guo, Z., Xia, Y., Ferreira, V.G., Liu, S., Wang, K., Yao, Y., Zhang, X., Zhao, C., 2019. Evaluation of twelve evapotranspiration products from machine learning, remote sensing and land surface models over conterminous United States. J. Hydrol. 578, 124105.

Yang, Y., Chen, R., Song, Y., Han, C., Liu, J., Liu, Z., 2019. Sensitivity of potential evapotranspiration to meteorological factors and their elevational gradients in the Qilian Mountains, northwestern. China. J. Hydrol. 568, 147–159.

Yang, Y., Shang, S., 2013. A hybrid dual-source scheme and trapezoid framework–based evapotranspiration model (HTEM) using satellite images: algorithm and model test. J. Geophys. Res.: Atmos. 118 (5), 2284–2300.

Yao, Y., Liang, S., Li, X., Hong, Y., Fisher, J.B., Zhang, N., Chen, J., Cheng, J., Zhao, S., Zhang, X., 2014. Bayesian multimodel estimation of global terrestrial latent heat flux from eddy covariance, meteorological, and satellite observations. J. Geophys. Res.: Atmos. 119 (8), 4521–4545.

Yoon, Y., Kumar, S.V., Forman, B.A., Zaitchik, B.F., Kwon, Y., Qian, Y., Rupper, S., Maggioni, V., Houser, P., Kirschbaum, D., 2019. Evaluating the uncertainty of terrestrial water budget components over high mountain. Asia. Front. Earth Sci. 7, 120.

Zhang, S., Li, X., She, J., Peng, X., 2019. Assimilating remote sensing data into GIS-based all sky solar radiation modeling for mountain terrain. Remote Sens. Environ. 231, 111239.

Zhao, M., Wang, W., Ma, Z., Wang, Q., Wang, Z., Chen, L., Fu, B., 2021. Soil water dynamics based on a contrastive experiment between vegetated and non-vegetated sites in a semiarid region in Northwest China. J. Hydrol. 603, 126880.